Two-dimensional central-upwind schemes for curvilinear grids and application to gas dynamics with angular momentum

Tobias F. Illenseer [a,*], Wolfgang J. Duschl [a,b]

[a] *Institut für Theoretische Physik und Astrophysik, Leibnizstrasse 15, D-24118 Kiel, Christian-Albrechts-Universität zu Kiel, Germany*
[b] *Steward Observatory, The University of Arizona, Tucson, Arizona 85721-0065, United States*

ARTICLE INFO

ABSTRACT

In this work we present new second order semi-discrete central schemes for systems of hyperbolic conservation laws on curvilinear grids. Our methods generalise the two-dimensional central-upwind schemes developed by Kurganov and Tadmor [A. Kurganov, E. Tadmor, Numer. Methods Partial Differential Equations 18 (2002) 584. [1]]. In these schemes we account for area and volume changes in the numerical flux functions due to the non-cartesian geometries. In case of vectorial conservation laws we introduce a general prescription of the geometrical source terms valid for various orthogonal curvilinear coordinate systems. The methods are applied to the two-dimensional Euler equations of inviscid gas dynamics with and without angular momentum transport. In the latter case we introduce a new test problem to examine the detailed conservation of specific angular momentum.

1. Introduction

In the last decades various multidimensional numerical schemes for the solution of hyperbolic conservation laws have been developed. The continuous increase in computing power provides the opportunity to perform accurate computations even in the case of three-dimensional problems. However, for some physical systems this might not be the appropriate approach. In cases where the underlying physics exhibit some kind of symmetry more accuracy can be achieved by omitting the dependence on one dimension. In some cases these symmetries might lead to different conservation laws. For instance in rotationally symmetric inviscid fluids angular momentum is locally conserved.

Among the variety of numerical methods the family of Godunov-type schemes are a very useful approach. Since the seminal work of Godunov [2] these schemes became an important tool in the numerical analysis of hyperbolic conservations laws. The original proposition of Godunov was quite simple: Approximate the initial condition by piecewise constant data. Then advance the solution in time by solving the intermittent local Riemann problems. Since those days the method was improved by introducing less time-consuming approximate Riemann-solvers. Furthermore the development of higher-order methods yields better convergence of the numerical schemes. In most parts of our report we will follow the work of Kurganov and Tadmor [1,3]. They proposed Riemann-solvers-free second order methods which avoid computation of the eigensystem of the advection problem. We incorporate orthogonal curvilinear coordinate systems into their cartesian scheme and therefore allow for area and volume changes of the grid cells.

The outline of our paper is as follows: In Section 1.1 we briefly review the covariant formulation of conservation laws and derive the basic two-dimensional integral equation for general orthogonal coordinates. This result is utilised in Section 2 to obtain second order semi-discrete non-oscillating numerical schemes resembling those described in [1]. In Section 3 we present the results of numerical computations obtained with the new scheme for the equations of gas dynamics. The simulations were carried out on curvilinear meshes and on a two-dimensional cartesian mesh for comparison. These tests examine the solution of two-dimensional Riemann problems in

---

polar and cylindrical geometry. In addition to that we introduce a method for testing the detailed conservation of angular momentum for rotationally symmetric flows in Section 3.3. Finally a summary is given in Section 4.

1.1. Conservation laws and orthogonal curvilinear coordinate systems

The concept of conservation is fundamental to a variety of physical phenomena and leads to partial differential equations of almost the same kind in very different areas. In this work we will focus on systems of non-linear hyperbolic conservation laws of the form

$$\frac{\partial u}{\partial t} + \nabla \cdot T(u) = 0. \tag{1.1}$$

Here u is either a scalar or vector and T a vector or rank-2 tensor. $\nabla\cdot$ denotes the covariant derivative with respect to some affine connection followed by a contraction over the last indices. In the following we will restrict ourselves to orthogonal curvilinear coordinates $\{\xi, \eta, \phi\}$ with a local orthonormal basis $\{\widehat{e}_{\hat{\xi}}, \widehat{e}_{\hat{\eta}}, \widehat{e}_{\hat{\phi}}\}$ and metric scale factors $\{h_\xi, h_\eta, h_\phi\}$. For the divergence of vector fields one obtains for all components with respect to local orthonormal frames

$$\nabla \cdot v = \frac{1}{\sqrt{g}} \left(\frac{\partial}{\partial \xi} (h_\eta h_\phi v_{\hat{\xi}}) + \frac{\partial}{\partial \eta} (h_\xi h_\phi v_{\hat{\eta}}) + \frac{\partial}{\partial \phi} (h_\xi h_\eta v_{\hat{\phi}}) \right) \tag{1.2}$$

and in case of tensor fields

$$[\nabla \cdot T]_{\hat{\xi}} = \frac{1}{\sqrt{g}} \left(\frac{\partial}{\partial \xi} (h_\eta h_\phi T_{\hat{\xi}\hat{\xi}}) + \frac{\partial}{\partial \eta} (h_\xi h_\phi T_{\hat{\xi}\hat{\eta}}) + \frac{\partial}{\partial \phi} (h_\xi h_\eta T_{\hat{\xi}\hat{\phi}}) \right) - c_{\hat{\eta}\hat{\xi}\hat{\eta}} T_{\hat{\eta}\hat{\eta}} - c_{\hat{\phi}\hat{\xi}\hat{\phi}} T_{\hat{\phi}\hat{\phi}} + c_{\hat{\xi}\hat{\eta}\hat{\xi}} T_{\hat{\eta}\hat{\xi}} + c_{\hat{\xi}\hat{\phi}\hat{\xi}} T_{\hat{\phi}\hat{\xi}},$$

$$[\nabla \cdot T]_{\hat{\eta}} = \frac{1}{\sqrt{g}} \left(\frac{\partial}{\partial \xi} (h_\eta h_\phi T_{\hat{\eta}\hat{\xi}}) + \frac{\partial}{\partial \eta} (h_\xi h_\phi T_{\hat{\eta}\hat{\eta}}) + \frac{\partial}{\partial \phi} (h_\xi h_\eta T_{\hat{\eta}\hat{\phi}}) \right) - c_{\hat{\xi}\hat{\eta}\hat{\xi}} T_{\hat{\xi}\hat{\xi}} - c_{\hat{\phi}\hat{\eta}\hat{\phi}} T_{\hat{\phi}\hat{\phi}} + c_{\hat{\eta}\hat{\xi}\hat{\eta}} T_{\hat{\xi}\hat{\eta}} + c_{\hat{\eta}\hat{\phi}\hat{\eta}} T_{\hat{\phi}\hat{\eta}},$$

$$[\nabla \cdot T]_{\hat{\phi}} = \frac{1}{\sqrt{g}} \left(\frac{\partial}{\partial \xi} (h_\eta h_\phi T_{\hat{\phi}\hat{\xi}}) + \frac{\partial}{\partial \eta} (h_\xi h_\phi T_{\hat{\phi}\hat{\eta}}) + \frac{\partial}{\partial \phi} (h_\xi h_\eta T_{\hat{\phi}\hat{\phi}}) \right) - c_{\hat{\xi}\hat{\phi}\hat{\xi}} T_{\hat{\xi}\hat{\xi}} - c_{\hat{\eta}\hat{\phi}\hat{\eta}} T_{\hat{\eta}\hat{\eta}} + c_{\hat{\phi}\hat{\xi}\hat{\phi}} T_{\hat{\xi}\hat{\phi}} + c_{\hat{\phi}\hat{\eta}\hat{\phi}} T_{\hat{\eta}\hat{\phi}}. \tag{1.3}$$

In these equations new geometrical quantities arise: The square root of the metric determinant $\sqrt{g} = h_\xi h_\eta h_\phi$ and the commutator coefficients c_{ijk} which depend on the metric scale factors and their derivatives. A more detailed derivation is given in Appendix A.

In this paper we will focus on two-dimensional conservation laws by assuming a coordinate symmetry with respect to ϕ. We may consider the 3D case in a follow-up paper. Hence we demand that all functions – geometrical scale factors as well as physical quantities – are independent of ϕ. Therefore the commutator coefficients with $\hat{\phi}$ in their second index vanish and a two-dimensional conservation law is obtained for the scalar variable u and vector field $v(u)$

$$\frac{\partial u}{\partial t} + \frac{1}{\sqrt{g}} \left(\frac{\partial}{\partial \xi} \left(h_\eta h_\phi v_{\hat{\xi}}(u) \right) + \frac{\partial}{\partial \eta} \left(h_\xi h_\phi v_{\hat{\eta}}(u) \right) \right) = 0. \tag{1.4}$$

In the same way we derive a vectorial conservation law for the vector w and tensor field $T(w)$

$$\frac{\partial w_{\hat{\xi}}}{\partial t} + \frac{1}{\sqrt{g}} \left(\frac{\partial}{\partial \xi} \left(h_\eta h_\phi T_{\hat{\xi}\hat{\xi}}(w) \right) + \frac{\partial}{\partial \eta} \left(h_\xi h_\phi T_{\hat{\xi}\hat{\eta}}(w) \right) \right) = c_{\hat{\eta}\hat{\xi}\hat{\eta}} T_{\hat{\eta}\hat{\eta}}(w) + c_{\hat{\phi}\hat{\xi}\hat{\phi}} T_{\hat{\phi}\hat{\phi}}(w) - c_{\hat{\xi}\hat{\eta}\hat{\xi}} T_{\hat{\eta}\hat{\xi}}(w),$$

$$\frac{\partial w_{\hat{\eta}}}{\partial t} + \frac{1}{\sqrt{g}} \left(\frac{\partial}{\partial \xi} \left(h_\eta h_\phi T_{\hat{\eta}\hat{\xi}}(w) \right) + \frac{\partial}{\partial \eta} \left(h_\xi h_\phi T_{\hat{\eta}\hat{\eta}}(w) \right) \right) = c_{\hat{\xi}\hat{\eta}\hat{\xi}} T_{\hat{\xi}\hat{\xi}}(w) + c_{\hat{\phi}\hat{\eta}\hat{\phi}} T_{\hat{\phi}\hat{\phi}}(w) - c_{\hat{\eta}\hat{\xi}\hat{\eta}} T_{\hat{\xi}\hat{\eta}}(w),$$

$$\frac{\partial w_{\hat{\phi}}}{\partial t} + \frac{1}{\sqrt{g}} \left(\frac{\partial}{\partial \xi} \left(h_\eta h_\phi T_{\hat{\phi}\hat{\xi}}(w) \right) + \frac{\partial}{\partial \eta} \left(h_\xi h_\phi T_{\hat{\phi}\hat{\eta}}(w) \right) \right) = -c_{\hat{\phi}\hat{\xi}\hat{\phi}} T_{\hat{\xi}\hat{\phi}}(w) - c_{\hat{\phi}\hat{\eta}\hat{\phi}} T_{\hat{\eta}\hat{\phi}}(w). \tag{1.5}$$

The only differences between scalar and vectorial conservation laws are the geometrical source terms in case of the latter. Therefore we can combine both to a system of conservation laws. At this point it is convenient to define new spatial differential operators

$$\mathcal{D}_\xi = \frac{1}{\sqrt{g}} \frac{\partial}{\partial \xi} h_\eta h_\phi, \qquad \mathcal{D}_\eta = \frac{1}{\sqrt{g}} \frac{\partial}{\partial \eta} h_\xi h_\phi \tag{1.6}$$

and rewrite the conservation law

$$\partial_t u + \mathcal{D}_\xi F(u) + \mathcal{D}_\eta G(u) = S(u). \tag{1.7}$$

In this compact notation u denotes the vector of conservative variables, $F(u)$, $G(u)$ and $S(u)$ are the flux vectors and geometrical source terms, respectively.

To allow for discontinuous solutions one integrates the differential equation (1.7) over the time interval $[t_n, t_{n+1}]$ and a spatial region D given by the cartesian product $[\xi_-, \xi_+] \times [\eta_-, \eta_+]$. Hence we obtain an integral equation, the so-called *weak formulation*

$$\left\langle u(t_{n+1}) \right\rangle_D = \left\langle u(t_n) \right\rangle_D - \int\limits_{t_n}^{t_{n+1}} \left\langle \mathcal{D}_\xi F + \mathcal{D}_\eta G - S \right\rangle_D dt \tag{1.8}$$
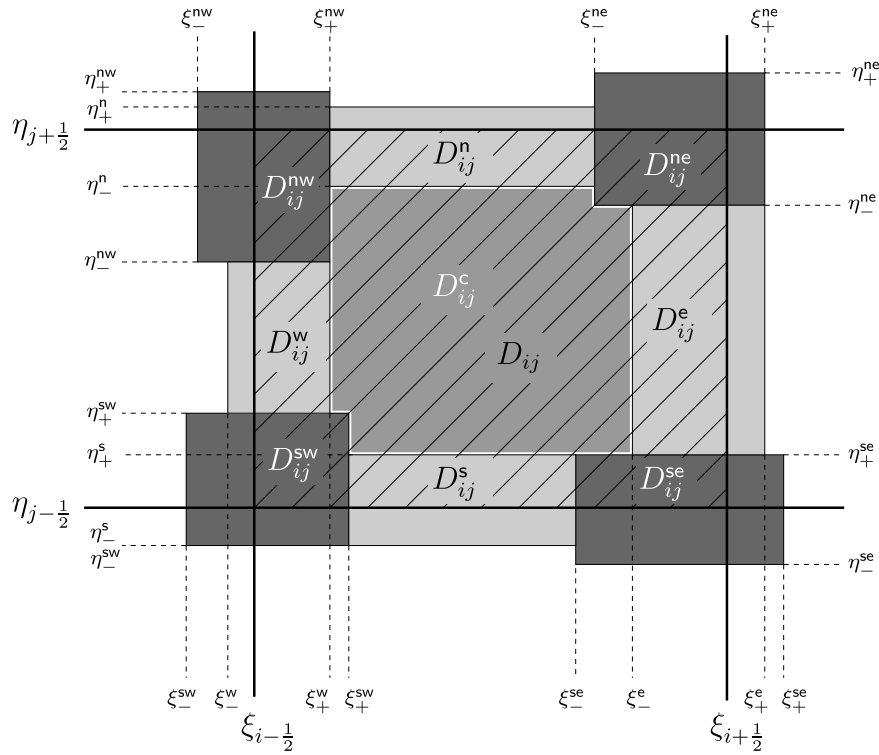
Fig. 2.1. Schematic view of the control volume.

using the notation $\langle\rangle$ for volume[1] averages as defined in

$$\big\langle X(t)\big\rangle_D = \frac{1}{\Delta V} \int\limits_{\xi_-}^{\xi_+} \int\limits_{\eta_-}^{\eta_+} X(t,\xi,\eta)\sqrt{g}\,\mathrm{d}\xi\,\mathrm{d}\eta \tag{1.9}$$

with spatial volume ΔV of region D

$$\Delta V = \int\limits_D \mathrm{d}V = \int\limits_{\xi_-}^{\xi_+} \int\limits_{\eta_-}^{\eta_+} \sqrt{g}\,\mathrm{d}\xi\,\mathrm{d}\eta. \tag{1.10}$$

Eq. (1.8) describes the time evolution of volume averaged conservative variables u in region D. So far it is impossible to evaluate the flux integrals without further knowledge of the function $u(t,\xi,\eta)$ on the surface of D and at time t within the interval $[t_n, t_{n+1}]$. However, in the next section we will derive a numerical scheme which provides an approximation to these integrals.

2. Numerical scheme

2.1. Semi-discrete scheme for generalised orthogonal coordinates

The derivation of the numerical scheme follows the three steps of reconstruction, evolution and projection described in [1]. For illustration consider the control volume selected by the cartesian product $D_{i,j} = [\xi_{i-\frac{1}{2}}, \xi_{i+\frac{1}{2}}] \times [\eta_{j-\frac{1}{2}}, \eta_{j+\frac{1}{2}}]$ in curvilinear orthogonal coordinates shown in Fig. 2.1. There are two types of staggered grid cells drawn along the boundary:

Edge cells are defined by the set union of partial regions at the edge of two adjacent cells (light grey in Fig. 2.1), e.g. at the eastern boundary:

$$D_{i+\frac{1}{2},j} = D_{i,j}^{\mathrm{e}} \cup D_{i+1,j}^{\mathrm{w}}$$

whereas the partial areas addressed by the index pair $\{i, j\}$ are given by

$$D_{i,j}^{\mathrm{w}} = \big[\xi_{i-\frac{1}{2}}, \xi_+^{\mathrm{w}}\big] \times \big[\eta_+^{\mathrm{sw}}, \eta_-^{\mathrm{nw}}\big], \qquad D_{i,j}^{\mathrm{e}} = \big[\xi_-^{\mathrm{e}}, \xi_{i+\frac{1}{2}}\big] \times \big[\eta_+^{\mathrm{se}}, \eta_-^{\mathrm{ne}}\big],$$
$$D_{i,j}^{\mathrm{s}} = \big[\xi_+^{\mathrm{sw}}, \xi_-^{\mathrm{se}}\big] \times \big[\eta_{j-\frac{1}{2}}, \eta_+^{\mathrm{s}}\big], \qquad D_{i,j}^{\mathrm{n}} = \big[\xi_+^{\mathrm{nw}}, \xi_-^{\mathrm{ne}}\big] \times \big[\eta_-^{\mathrm{n}}, \eta_{j+\frac{1}{2}}\big].$$

---

[1] The integration with respect to ϕ is suppressed throughout the whole paper, because all functions are considered independent of ϕ. Nevertheless we will stick to the term "volume" for integrals over two-dimensional domains.

Corner cells are formed by the partial regions of the four neighboring cells which meet in a cells corner (dark grey in Fig. 2.1), e.g. around the south-eastern corner:

$$D_{i+\frac{1}{2},j-\frac{1}{2}} = D_{i,j}^{se} \cup D_{i+1,j}^{sw} \cup D_{i,j-1}^{ne} \cup D_{i+1,j-1}^{nw}.$$

With the help of the definition of all partial corner areas with respect to cell $\{i, j\}$

$$D_{i,j}^{sw} = \left[\xi_{i-\frac{1}{2}}, \xi_+^{sw}\right] \times \left[\eta_{j-\frac{1}{2}}, \eta_+^{sw}\right], \qquad D_{i,j}^{se} = \left[\xi_-^{se}, \xi_{i+\frac{1}{2}}\right] \times \left[\eta_{j-\frac{1}{2}}, \eta_+^{se}\right],$$

$$D_{i,j}^{nw} = \left[\xi_{i-\frac{1}{2}}, \xi_+^{nw}\right] \times \left[\eta_-^{nw}, \eta_{j+\frac{1}{2}}\right], \qquad D_{i,j}^{ne} = \left[\xi_-^{ne}, \xi_{i+\frac{1}{2}}\right] \times [\eta_-^{ne}, \eta_{j+\frac{1}{2}}].$$

it is possible to construct the staggered corner cells.

Central region: Finally the remaining central region of the cell is defined by the complement

$$D_{i,j}^{c} = \overline{\left(D_{i,j} \cap \bigcup_{\alpha \in \{w,e,s,n,sw,se,nw,ne\}} D_{i,j}^{\alpha}\right)}. \tag{2.1}$$

For the derivation of the numerical scheme we assume that at time t_n volume averages of the conservative variables $u_{i,j}^n := \langle u(t_n) \rangle_{D_{i,j}}$ are available for each cell in the computational domain. Cell boundary data is obtained via piecewise linear reconstruction. Using cell mean values and proper approximations for the slopes the linear expansion yields

$$\widetilde{u}_{i,j}^n(\xi, \eta) = u_{i,j}^n + (\partial_\xi u)_{i,j}^n(\xi - \xi_0) + (\partial_\eta u)_{i,j}^n(\eta - \eta_0), \tag{2.2}$$

with $\xi, \xi_0 \in [\xi_{i-\frac{1}{2}}, \xi_{i+\frac{1}{2}}]$ and $\eta, \eta_0 \in [\eta_{j-\frac{1}{2}}, \eta_{j+\frac{1}{2}}]$. It is essential to deplete artificial oscillations caused by this linear reconstruction process in order to obtain stability for second order numerical schemes. Various methods are discussed in the literature to achieve stable non-oscillating second order schemes, see e.g. [4–7]. The original scheme by Kurganov and Tadmor follows the MUSCL (*Monotone Upstream-centred Schemes for Conservation Laws*) approach first proposed by van Leer [8]. This method introduces non-linear functions – so-called (slope) limiters – to damp spurious oscillations. The method may also apply to a curvilinear scheme, if one demands consistency with the averaging process

$$\langle \widetilde{u}_{i,j}^n \rangle_{D_{i,j}} = \langle u(t_n) \rangle_{D_{i,j}} = u_{i,j}^n. \tag{2.3}$$

This equation should hold independently of the actual choice for the slopes. Mönchmeyer and Müller [9] showed that this property is essential to retain a conservative scheme in case of non-cartesian grids (see also [10]). With help of Eq. (2.3) one derives the corollary that the coordinate pair (ξ_0, η_0) is determined by the barycentre of each control volume

$$\xi_0 = \langle \xi \rangle_{D_{i,j}}, \qquad \eta_0 = \langle \eta \rangle_{D_{i,j}}. \tag{2.4}$$

Therefore cell mean values might be regarded as point values at the barycentre. Eq. (2.2) together with an integral conservation law for all the staggered grid cells similar to (1.8) forms the building block to advance the solution in time. As an intermediate result one computes cell mean values at time t_{n+1} defined on the staggered grid. Finally the updated mean values are obtained by reconstructing the staggered data and projecting these functions onto the original cell area $D_{i,j}$

$$u_{i,j}^{n+1} = \frac{1}{\Delta V_{i,j}} \int_{D_{i,j}} \widetilde{w}^{n+1}(\xi, \eta) \, dV = \langle \widetilde{w}^{n+1} \rangle_{D_{i,j}}. \tag{2.5}$$

This is the generalised formulation of Eq. (2.3) in [1] for orthogonal curvilinear coordinates. The function $\widetilde{w}^{n+1}(\xi, \eta)$ refers to the combination of piecewise linear reconstructions on the staggered grid. Depending on the control volume in which they are defined this function may vary from cell to cell. Nevertheless one can subdivide the integration into parts carried out over regions determined by the intersection of $D_{i,j}$ with the staggered cells (cf. Fig. 2.1)

$$u_{i,j}^{n+1} = \frac{1}{\Delta V_{i,j}} \left(\sum_{\alpha \in \{w,e,s,n\}} \Delta V_{i,j}^{\alpha} \langle \widetilde{w}_\alpha^{n+1} \rangle_{D_{i,j}^\alpha} + \sum_{\beta \in \{sw,se,nw,ne\}} \Delta V_{i,j}^{\beta} \langle \widetilde{w}_\beta^{n+1} \rangle_{D_{i,j}^\beta} + \Delta V_{i,j}^{c} \langle \widetilde{w}_c^{n+1} \rangle_{D_{i,j}^c} \right). \tag{2.6}$$

Up to this point no information about the advection problem has entered our considerations. This changes if we fix the limits for integration by introducing the minimal and maximal local speeds of propagation for discontinuities according to [11], e.g. at the western and eastern cell boundaries

$$a_{i\pm\frac{1}{2},j}^{+} = \max_{\omega \in \mathcal{C}(u_{i\pm\frac{1}{2},j}^{+}, u_{i\pm\frac{1}{2},j}^{-})} \left\{ \lambda_{\max}\left(\frac{\partial F}{\partial u}(\omega)\right), 0 \right\},$$

$$a_{i\pm\frac{1}{2},j}^{-} = \min_{\omega \in \mathcal{C}(u_{i\pm\frac{1}{2},j}^{+}, u_{i\pm\frac{1}{2},j}^{-})} \left\{ \lambda_{\min}\left(\frac{\partial F}{\partial u}(\omega)\right), 0 \right\}. \tag{2.7}$$

Here $\mathcal{C}$ denotes a curve in phase space connecting two adjacent states $u_{i-\frac{1}{2},j}^{+}$ and $u_{i-\frac{1}{2},j}^{-}$ of neighboring cells via the Riemann fan and $\lambda_{\min}, \lambda_{\max}$ the minimal and maximal eigenvalue of the Jacobian $\left(\frac{\partial F}{\partial u}\right)$. Similar definitions apply to the southern $b_{i,j-\frac{1}{2}}^{\pm}$ and northern $b_{i,j+\frac{1}{2}}^{\pm}$

wave speeds with the exception that the Jacobian of F has to be replaced by $\left(\frac{\partial G}{\partial u}\right)$. Although these expressions seem to be difficult to evaluate, for genuinely non-linear or linearly degenerate waves it is sufficient to compute (cf. [11])

$$
\begin{aligned}
a^+_{i\pm\frac{1}{2},j} &= \max\left\{\lambda_{\max}\left(\frac{\partial F}{\partial u}\left(u^+_{i\pm\frac{1}{2},j}\right)\right), \lambda_{\max}\left(\frac{\partial F}{\partial u}\left(u^-_{i\pm\frac{1}{2},j}\right)\right), 0\right\}, \\
a^-_{i\pm\frac{1}{2},j} &= \min\left\{\lambda_{\min}\left(\frac{\partial F}{\partial u}\left(u^+_{i\pm\frac{1}{2},j}\right)\right), \lambda_{\min}\left(\frac{\partial F}{\partial u}\left(u^-_{i\pm\frac{1}{2},j}\right)\right), 0\right\}.
\end{aligned}
\tag{2.8}
$$

This is strictly true only for cartesian coordinates. The reason for this limitation is that the underlying formalism is based on the characteristic decomposition of the quasi-linear conservation law. In cartesian coordinates the transformation to a quasi-linear form is straightforward. A simple calculation with help of the chain rule yields

$$
\frac{\partial u}{\partial t} + \left(\frac{\partial F}{\partial u}\right)\frac{\partial u}{\partial x} + \left(\frac{\partial G}{\partial u}\right)\frac{\partial u}{\partial y} = 0.
$$

However, the curvilinear advection operators (1.6) involve derivatives of geometrical scale factors and the quasi-linear conservation law becomes

$$
\partial_t u + \left(\frac{\partial F}{\partial u}\right)\mathcal{D}_\xi u + \left(\frac{\partial G}{\partial u}\right)\mathcal{D}_\eta u = S(u).
\tag{2.9}
$$

This is equivalent to Eq. (1.7) if and only if the flux functions F and G are homogeneous functions of the conservative variables u. For a homogeneous function

$$
F(u) = \left(\frac{\partial F}{\partial u}\right)u
$$

holds (cf. [12], Ch. 16.2). Hence

$$
\mathcal{D}_\xi F(u) = \frac{1}{\sqrt{g}}\frac{\partial}{\partial\xi}\left(h_\eta h_\phi F(u)\right) = \frac{1}{\sqrt{g}}\frac{\partial}{\partial\xi}(h_\xi h_\eta)\left(\frac{\partial F}{\partial u}\right)u + \frac{h_\xi h_\eta}{\sqrt{g}}\left(\frac{\partial F}{\partial u}\right)\frac{\partial u}{\partial\xi} = \left(\frac{\partial F}{\partial u}\right)\frac{1}{\sqrt{g}}\frac{\partial}{\partial\xi}(h_\eta h_\phi u) = \left(\frac{\partial F}{\partial u}\right)\mathcal{D}_\xi u
$$

and (1.7) may be rewritten in the quasi-linear form (2.9). Apart from this discrepancy there is another pitfall when using curvilinear coordinates. The extent of the staggered grid cells is computed via multiplication of the local propagation speeds with the time step Δt. However, in curvilinear coordinates spatial distances are not equal to coordinate distances. Therefore proper distances should be obtained via evaluation of path integrals in compliance with

$$
\int_{\xi_{i\pm\frac{1}{2}}}^{\xi^{w,e}_\pm} h_\xi(\xi,\eta)\,\mathrm{d}\xi \approx h_\xi(\xi_{i\pm\frac{1}{2}},\eta)\left(\xi^{w,e}_\pm - \xi_{i\pm\frac{1}{2}}\right), \qquad \int_{\eta_{j\pm\frac{1}{2}}}^{\eta^{s,n}_\pm} h_\eta(\xi,\eta)\,\mathrm{d}\eta \approx h_\eta(\xi,\eta_{j\pm\frac{1}{2}})\left(\eta^{s,n}_\pm - \eta_{j\pm\frac{1}{2}}\right).
\tag{2.10}
$$

The accuracy of the approximations is sufficient as long as the coordinate distance is small enough. In fact in the limit $\Delta t \to 0$ the staggered grid cells will collapse to lines, so that the considerations will hold. Hence the limits of staggered zones along the edges with respect to cell $D_{i,j}$ are given by

$$
\begin{aligned}
\xi^w_- &= \xi_{i-\frac{1}{2}} + \frac{a^-_{i-\frac{1}{2},j}\Delta t}{h_\xi(\xi_{i-\frac{1}{2}},\eta)}, & \xi^w_+ &= \xi_{i-\frac{1}{2}} + \frac{a^+_{i-\frac{1}{2},j}\Delta t}{h_\xi(\xi_{i-\frac{1}{2}},\eta)}, \\
\xi^e_- &= \xi_{i+\frac{1}{2}} + \frac{a^-_{i+\frac{1}{2},j}\Delta t}{h_\xi(\xi_{i+\frac{1}{2}},\eta)}, & \xi^e_+ &= \xi_{i+\frac{1}{2}} + \frac{a^+_{i+\frac{1}{2},j}\Delta t}{h_\xi(\xi_{i+\frac{1}{2}},\eta)}, \\
\eta^s_- &= \eta_{j-\frac{1}{2}} + \frac{b^-_{i,j-\frac{1}{2}}\Delta t}{h_\eta(\xi,\eta_{j-\frac{1}{2}})}, & \eta^s_+ &= \eta_{j-\frac{1}{2}} + \frac{b^+_{i,j-\frac{1}{2}}\Delta t}{h_\eta(\xi,\eta_{j-\frac{1}{2}})}, \\
\eta^n_- &= \eta_{j+\frac{1}{2}} + \frac{b^-_{i,j+\frac{1}{2}}\Delta t}{h_\eta(\xi,\eta_{j+\frac{1}{2}})}, & \eta^n_+ &= \eta_{j+\frac{1}{2}} + \frac{b^+_{i,j+\frac{1}{2}}\Delta t}{h_\eta(\xi,\eta_{j+\frac{1}{2}})}.
\end{aligned}
\tag{2.11}
$$

Whereas in the corners one computes

$$\xi_+^{\text{sw}} = \xi_{i-\frac{1}{2}} + \frac{A_{i-\frac{1}{2},j-\frac{1}{2}}^+ \Delta t}{h_\xi(\xi_{i-\frac{1}{2}},\eta)}, \qquad \xi_-^{\text{se}} = \xi_{i+\frac{1}{2}} + \frac{A_{i+\frac{1}{2},j-\frac{1}{2}}^- \Delta t}{h_\xi(\xi_{i+\frac{1}{2}},\eta)},$$

$$\xi_+^{\text{nw}} = \xi_{i-\frac{1}{2}} + \frac{A_{i-\frac{1}{2},j+\frac{1}{2}}^+ \Delta t}{h_\xi(\xi_{i-\frac{1}{2}},\eta)}, \qquad \xi_-^{\text{ne}} = \xi_{i+\frac{1}{2}} + \frac{A_{i+\frac{1}{2},j+\frac{1}{2}}^- \Delta t}{h_\xi(\xi_{i+\frac{1}{2}},\eta)},$$

$$\eta_+^{\text{sw}} = \eta_{j-\frac{1}{2}} + \frac{B_{i-\frac{1}{2},j-\frac{1}{2}}^+ \Delta t}{h_\eta(\xi,\eta_{j-\frac{1}{2}})}, \qquad \eta_-^{\text{nw}} = \eta_{j+\frac{1}{2}} + \frac{B_{i-\frac{1}{2},j+\frac{1}{2}}^- \Delta t}{h_\eta(\xi,\eta_{j+\frac{1}{2}})},$$

$$\eta_+^{\text{se}} = \eta_{j-\frac{1}{2}} + \frac{B_{i-\frac{1}{2},j+\frac{1}{2}}^+ \Delta t}{h_\eta(\xi,\eta_{j-\frac{1}{2}})}, \qquad \eta_-^{\text{ne}} = \eta_{j+\frac{1}{2}} + \frac{B_{i+\frac{1}{2},j+\frac{1}{2}}^- \Delta t}{h_\eta(\xi,\eta_{j+\frac{1}{2}})}. \tag{2.12}$$

Here the propagation speeds are derived from the values of neighboring cells according to (see [11])

$$A_{i\pm\frac{1}{2},j-\frac{1}{2}}^+ = \max\{a_{i\pm\frac{1}{2},j}^+, a_{i\pm\frac{1}{2},j-1}^+\}, \qquad A_{i\pm\frac{1}{2},j-\frac{1}{2}}^- = \min\{a_{i\pm\frac{1}{2},j}^-, a_{i\pm\frac{1}{2},j-1}^-\},$$

$$A_{i\pm\frac{1}{2},j+\frac{1}{2}}^+ = \max\{a_{i\pm\frac{1}{2},j}^+, a_{i\pm\frac{1}{2},j+1}^+\}, \qquad A_{i\pm\frac{1}{2},j+\frac{1}{2}}^- = \min\{a_{i\pm\frac{1}{2},j}^-, a_{i\pm\frac{1}{2},j+1}^-\},$$

$$B_{i-\frac{1}{2},j\pm\frac{1}{2}}^+ = \max\{b_{i,j\pm\frac{1}{2}}^+, b_{i-1,j\pm\frac{1}{2}}^+\}, \qquad B_{i-\frac{1}{2},j\pm\frac{1}{2}}^- = \min\{b_{i,j\pm\frac{1}{2}}^-, b_{i-1,j\pm\frac{1}{2}}^-\},$$

$$B_{i+\frac{1}{2},j\pm\frac{1}{2}}^+ = \max\{b_{i,j\pm\frac{1}{2}}^+, b_{i+1,j\pm\frac{1}{2}}^+\}, \qquad B_{i+\frac{1}{2},j\pm\frac{1}{2}}^- = \min\{b_{i,j\pm\frac{1}{2}}^-, b_{i+1,j\pm\frac{1}{2}}^-\}. \tag{2.13}$$

With these definitions we may expand the integrals over staggered cells arising in (2.6), e.g. for the southern domain $D_{i,j}^{\text{s}}$ the integral of an arbitrary function $f(\xi,\eta)$ is given by

$$\int\limits_{D_{i,j}^{\text{s}}} f(\xi,\eta)\,\mathrm{d}V = \int\limits_{\eta_{j-\frac{1}{2}}}^{\eta_+^{\text{s}}} \int\limits_{\xi_+^{\text{sw}}}^{\xi_-^{\text{se}}} f(\xi,\eta)h_\xi h_\eta h_\phi\,\mathrm{d}\xi\,\mathrm{d}\eta = \int\limits_{\xi_+^{\text{sw}}}^{\xi_-^{\text{se}}} f(\xi,\eta)h_\xi h_\eta h_\phi\big(\eta_+^{\text{s}} - \eta_{j-\frac{1}{2}}\big)\,\mathrm{d}\xi\bigg|_{\eta_{j-\frac{1}{2}}} + \mathcal{O}\big((\eta_+^{\text{s}} - \eta_{j-\frac{1}{2}})^2\big).$$

With the help of (2.11) this leads to

$$\int\limits_{D_{i,j}^{\text{s}}} f(\xi,\eta)\,\mathrm{d}V = b_{i,j-\frac{1}{2}}^+ \Delta t \int\limits_{\xi_+^{\text{sw}}}^{\xi_-^{\text{se}}} f(\xi,\eta)h_\xi h_\phi\,\mathrm{d}\xi\bigg|_{\eta_{j-\frac{1}{2}}} + \mathcal{O}\big(\Delta t^2\big). \tag{2.14}$$

Therefore the volume of the southern region may be expressed by

$$\Delta V_{i,j}^{\text{s}} = \int\limits_{D_{i,j}^{\text{s}}} \mathrm{d}V = b_{i,j-\frac{1}{2}}^+ \Delta t \int\limits_{\xi_+^{\text{sw}}}^{\xi_-^{\text{se}}} h_\xi h_\phi\,\mathrm{d}\xi\bigg|_{\eta_{j-\frac{1}{2}}} + \mathcal{O}\big(\Delta t^2\big). \tag{2.15}$$

Furthermore it is necessary to compute approximations for the flux integrals arising in (1.8), e.g. again for the southern domain this yields

$$\int\limits_{D_{i,j}^{\text{s}}} \mathcal{D}_\xi F\,\mathrm{d}V = b_{i,j-\frac{1}{2}}^+ \Delta t [h_\phi F]_{\xi_+^{\text{sw}},\eta_{j-\frac{1}{2}}}^{\xi_-^{\text{se}},\eta_{j-\frac{1}{2}}} + \mathcal{O}\big(\Delta t^2\big), \tag{2.16}$$

$$\int\limits_{D_{i,j}^{\text{s}}} \mathcal{D}_\eta G\,\mathrm{d}V = \left[\int\limits_{\xi_+^{\text{sw}}}^{\xi_-^{\text{se}}} h_\xi h_\phi G\,\mathrm{d}\xi\right]_{\eta_{j-\frac{1}{2}}}^{\eta_+^{\text{s}}}. \tag{2.17}$$

Similar equations can be obtained for the other staggered domains along the edges. We would like to emphasise that the dependence on Δt in these formulas is influenced by the choice for the slopes in the reconstruction formula (2.2). A more rigorous treatment given in [13] shows that some of the terms proportional to Δt might be of $\mathcal{O}(1)$. This has implications on the limiting process carried out at the end of this subsection leading to numerical fluxes with less numerical dissipation. To proceed with the derivation of the numerical scheme we expand the first sum in (2.6) up to first order in Δt using (2.14), (2.15)

$$\sum_{\alpha\in\{\text{w,e,s,n}\}} \Delta V_{i,j}^\alpha \langle\widetilde{w}_\alpha^{n+1}\rangle_{D_{i,j}^\alpha} = \Delta V_{i,j}^{\text{w}} w_{i-\frac{1}{2},j}^{n+1} + \Delta V_{i,j}^{\text{e}} w_{i+\frac{1}{2},j}^{n+1} + \Delta V_{i,j}^{\text{s}} w_{i,j-\frac{1}{2}}^{n+1} + \Delta V_{i,j}^{\text{n}} w_{i,j+\frac{1}{2}}^{n+1} + \mathcal{O}\big(\Delta t^2\big), \tag{2.18}$$

where $\widetilde{w}_\alpha^{n+1}$ denote the staggered reconstructions. They are defined in the same way as the non-staggered reconstructions, e.g. in the southern domain according to

$$\widetilde{w}_{\text{s}}^{n+1}(\xi,\eta) = \widetilde{w}_{i,j-\frac{1}{2}}^{n+1}(\xi,\eta)|_{\xi,\eta\in D_{i,j}^{\text{s}}} = w_{i,j-\frac{1}{2}}^{n+1} + (\partial_\xi w)_{i,j-\frac{1}{2}}^{n+1}(\xi - \xi_0) + (\partial_\eta w)_{i,j-\frac{1}{2}}^{n+1}(\eta - \eta_0), \tag{2.19}$$

with mean value $w_{i,j-\frac{1}{2}}^{n+1}$ in the staggered area $D_{i,j-\frac{1}{2}} = D_{i,j-1}^n \cup D_{i,j}^s$. We would like to emphasise that the cell barycentres (ξ_0, η_0) in Eq. (2.19) are not identical to those in Eq. (2.4) because they depend on the domain under consideration. As in the case of non-staggered reconstructions we demand consistency with the averaging process for all staggered reconstructions [see Eq. (2.3)], e.g. in the southern domain

$$\langle \widetilde{w}_{i,j-\frac{1}{2}}^{n+1} \rangle_{D_{i,j-\frac{1}{2}}} = w_{i,j-\frac{1}{2}}^{n+1}. \tag{2.20}$$

In case of the corner regions (second sum in (2.6)) one can avoid the detailed computations. A short calculation proves with help of Eq. (2.12) that all volume elements are of order Δt^2 (cf. [11]), e.g. for the north-western domain

$$\Delta V_{i,j}^{\mathrm{nw}} = \int_{D_{i,j}^{\mathrm{nw}}} \mathrm{d}V = \int_{\eta_-^{\mathrm{nw}}}^{\eta_{j+\frac{1}{2}}} \int_{\xi_{i-\frac{1}{2}}}^{\xi_+^{\mathrm{nw}}} h_\xi h_\eta h_\phi \, \mathrm{d}\xi \, \mathrm{d}\eta = \left(\eta_{j+\frac{1}{2}} - \eta_-^{\mathrm{nw}} \right) \left(\xi_+^{\mathrm{nw}} - \xi_{i-\frac{1}{2}} \right) h_\xi h_\eta h_\phi \big|_{\xi_{i-\frac{1}{2}}, \eta_{j+\frac{1}{2}}} + \mathcal{O}(\Delta t^4)$$

$$= -B_{i-\frac{1}{2}, j+\frac{1}{2}}^- A_{i-\frac{1}{2}, j+\frac{1}{2}}^+ \Delta t^2 h_\phi(\xi_{i-\frac{1}{2}}, \eta_{j+\frac{1}{2}}) + \mathcal{O}(\Delta t^4).$$

Therefore using piecewise linear reconstructions similar to those in (2.19) one concludes that

$$\sum_{\beta \in \{sw, se, nw, ne\}} \Delta V_{i,j}^\beta \langle \widetilde{w}_\beta^{n+1} \rangle_{D_{i,j}^\beta} = \mathcal{O}(\Delta t^2). \tag{2.21}$$

Henceforth one proceeds with the simplification of Eq. (2.6). The expressions (2.18), (2.21) replace the first and second sum of (2.6) and the updated cell mean values become

$$u_{i,j}^{n+1} = \frac{1}{\Delta V_{i,j}} \left(\Delta V_{i,j}^{\mathrm{w}} w_{i-\frac{1}{2}, j}^{n+1} + \Delta V_{i,j}^{\mathrm{e}} w_{i+\frac{1}{2}, j}^{n+1} + \Delta V_{i,j}^{\mathrm{s}} w_{i,j-\frac{1}{2}}^{n+1} + \Delta V_{i,j}^{\mathrm{n}} w_{i,j+\frac{1}{2}}^{n+1} + \Delta V_{i,j}^{\mathrm{c}} w_{i,j}^{n+1} \right) + \mathcal{O}(\Delta t^2). \tag{2.22}$$

Here we used a constraint similar to (2.20) applied to the central region to substitute $\langle \widetilde{w}_{\mathrm{c}}^{n+1} \rangle_{D_{i,j}^c}$ by the mean value $w_{i,j}^{n+1}$. The next step in the derivation of the update formula for cell mean values incorporates the integral form of the conservation law. With help of (1.8) one replaces the mean values on the staggered grid at time step t_{n+1} with flux and source term integrals. The integrals with respect to time may then be approximated by the midpoint quadrature rule. Hence for the central region one obtains

$$\Delta V_{i,j}^c w_{i,j}^{n+1} = \Delta V_{i,j}^c \left(\langle \widetilde{u}_{i,j}^n \rangle_{D_{i,j}^c} - \langle \mathcal{D}_\xi F + \mathcal{D}_\eta G - S \rangle_{D_{i,j}^c} \big|_{t_n + \frac{\Delta t}{2}} \Delta t + \mathcal{O}(\Delta t^2) \right).$$

To simplify integration over the irregular shaped domain $D_{i,j}^c$ one can substitute this integral with that over the whole cell area $D_{i,j}$ and subtract those integrals over the supplementary domains along the cell boundary (see (2.1))

$$\Delta V_{i,j}^c w_{i,j}^{n+1} = \Delta V_{i,j} \left\{ \langle \widetilde{u}_{i,j}^n \rangle_{D_{i,j}} - \langle \mathcal{D}_\xi F + \mathcal{D}_\eta G - S \rangle_{D_{i,j}} \big|_{t_n + \frac{\Delta t}{2}} \Delta t \right\}$$

$$- \sum_{\alpha \in \{w, e, s, n\}} \Delta V_{i,j}^\alpha \left\{ \langle \widetilde{u}_{i,j}^n \rangle_{D_{i,j}^\alpha} - \langle \mathcal{D}_\xi F + \mathcal{D}_\eta G - S \rangle_{D_{i,j}^\alpha} \big|_{t_n + \frac{\Delta t}{2}} \Delta t \right\} + \mathcal{O}(\Delta t^2).$$

Again it is safe to omit the integrals over the corner areas (see (2.21)). Since some of the flux integrals over edge domains are of order Δt (cf. Eqs. (2.16), (2.17),[2] multiplication with Δt again leads to terms of order Δt^2. Thus dropping all terms of order Δt^2 the contribution due to the central region reduces to

$$\Delta V_{i,j}^c w_{i,j}^{n+1} = \Delta V_{i,j} \left\{ \langle \widetilde{u}_{i,j}^n \rangle_{D_{i,j}} - \langle \mathcal{D}_\xi F + \mathcal{D}_\eta G - S \rangle_{D_{i,j}} \big|_{t_n + \frac{\Delta t}{2}} \Delta t \right\} - \sum_{\alpha \in \{w, e, s, n\}} \Delta V_{i,j}^\alpha \langle \widetilde{u}_{i,j}^n \rangle_{D_{i,j}^\alpha}$$

$$- \Delta t \left\{ \Delta V_{i,j}^{\mathrm{w}} \langle \mathcal{D}_\xi F \rangle_{D_{i,j}^{\mathrm{w}}} + \Delta V_{i,j}^{\mathrm{e}} \langle \mathcal{D}_\xi F \rangle_{D_{i,j}^{\mathrm{e}}} + \Delta V_{i,j}^{\mathrm{s}} \langle \mathcal{D}_\eta G \rangle_{D_{i,j}^{\mathrm{s}}} + \Delta V_{i,j}^{\mathrm{n}} \langle \mathcal{D}_\eta G \rangle_{D_{i,j}^{\mathrm{n}}} \right\} \big|_{t_n + \frac{\Delta t}{2}} + \mathcal{O}(\Delta t^2).$$

This result is completely determined by reconstructed data inside $D_{i,j}$ whereas for the staggered cells around the boundaries different reconstructions of adjacent cells have to be taken into account. The same argument regarding flux integrals over boundary areas as mentioned above applies in this case. Thus the cell mean values within the edge regions are determined by

$$w_{i\pm\frac{1}{2}, j}^{n+1} = \frac{1}{\Delta V_{i\pm\frac{1}{2}, j}} \left\{ \Delta V_{i,j}^{\mathrm{e(w)}} \left(\langle \widetilde{u}_{i,j}^n \rangle_{D_{i,j}^{\mathrm{e(w)}}} - \langle \mathcal{D}_\xi F \rangle_{D_{i,j}^{\mathrm{e(w)}}} \big|_{t_n + \frac{\Delta t}{2}} \Delta t \right) + \Delta V_{i\pm1, j}^{\mathrm{w(e)}} \left(\langle \widetilde{u}_{i\pm1, j}^n \rangle_{D_{i\pm1, j}^{\mathrm{w(e)}}} - \langle \mathcal{D}_\xi F \rangle_{D_{i\pm1, j}^{\mathrm{w(e)}}} \big|_{t_n + \frac{\Delta t}{2}} \Delta t \right) \right\} + \mathcal{O}(\Delta t^2),$$

$$w_{i, j\pm\frac{1}{2}}^{n+1} = \frac{1}{\Delta V_{i, j\pm\frac{1}{2}}} \left\{ \Delta V_{i,j}^{\mathrm{n(s)}} \left(\langle \widetilde{u}_{i,j}^n \rangle_{D_{i,j}^{\mathrm{n(s)}}} - \langle \mathcal{D}_\eta G \rangle_{D_{i,j}^{\mathrm{n(s)}}} \big|_{t_n + \frac{\Delta t}{2}} \Delta t \right) + \Delta V_{i, j\pm1}^{\mathrm{s(n)}} \left(\langle \widetilde{u}_{i, j\pm1}^n \rangle_{D_{i, j\pm1}^{\mathrm{n(s)}}} - \langle \mathcal{D}_\eta G \rangle_{D_{i, j\pm1}^{\mathrm{n(s)}}} \big|_{t_n + \frac{\Delta t}{2}} \Delta t \right) \right\} + \mathcal{O}(\Delta t^2).$$

---

[2] A different reconstruction causes some of the terms proportional to Δt to be of $\mathcal{O}(1)$ (see comments to Eq. (2.17)).

Insertion into (2.22) yields

$$
u_{i,j}^{n+1} = u_{i,j}^n - \langle \mathcal{D}_\xi F + \mathcal{D}_\eta G - S \rangle_{D_{i,j}} \big|_{t_n + \frac{\Delta t}{2}} \Delta t
$$

$$
- \frac{1}{\Delta V_{i,j}} \Bigg\{ \frac{\Delta V_{i,j}^{\mathrm{w}} \Delta V_{i-1,j}^{\mathrm{e}}}{\Delta V_{i-\frac{1}{2},j}} \Big(\langle \widetilde{u}_{i,j}^n \rangle_{D_{i,j}^{\mathrm{w}}} - \langle \mathcal{D}_\xi F \rangle_{D_{i,j}^{\mathrm{w}}} \big|_{t_n + \frac{\Delta t}{2}} \Delta t - \langle \widetilde{u}_{i-1,j}^n \rangle_{D_{i-1,j}^{\mathrm{e}}} + \langle \mathcal{D}_\xi F \rangle_{D_{i-1,j}^{\mathrm{e}}} \big|_{t_n + \frac{\Delta t}{2}} \Delta t \Big)
$$

$$
+ \frac{\Delta V_{i,j}^{\mathrm{e}} \Delta V_{i+1,j}^{\mathrm{w}}}{\Delta V_{i+\frac{1}{2},j}} \Big(\langle \widetilde{u}_{i,j}^n \rangle_{D_{i,j}^{\mathrm{e}}} - \langle \mathcal{D}_\xi F \rangle_{D_{i,j}^{\mathrm{e}}} \big|_{t_n + \frac{\Delta t}{2}} \Delta t - \langle \widetilde{u}_{i+1,j}^n \rangle_{D_{i+1,j}^{\mathrm{w}}} + \langle \mathcal{D}_\xi F \rangle_{D_{i+1,j}^{\mathrm{w}}} \big|_{t_n + \frac{\Delta t}{2}} \Delta t \Big)
$$

$$
+ \frac{\Delta V_{i,j}^{\mathrm{s}} \Delta V_{i,j-1}^{\mathrm{n}}}{\Delta V_{i,j-\frac{1}{2}}} \Big(\langle \widetilde{u}_{i,j}^n \rangle_{D_{i,j}^{\mathrm{s}}} - \langle \mathcal{D}_\eta G \rangle_{D_{i,j}^{\mathrm{s}}} \big|_{t_n + \frac{\Delta t}{2}} \Delta t - \langle \widetilde{u}_{i,j-1}^n \rangle_{D_{i,j-1}^{\mathrm{n}}} + \langle \mathcal{D}_\eta G \rangle_{D_{i,j-1}^{\mathrm{n}}} \big|_{t_n + \frac{\Delta t}{2}} \Delta t \Big)
$$

$$
+ \frac{\Delta V_{i,j}^{\mathrm{n}} \Delta V_{i,j+1}^{\mathrm{s}}}{\Delta V_{i,j+\frac{1}{2}}} \Big(\langle \widetilde{u}_{i,j}^n \rangle_{D_{i,j}^{\mathrm{n}}} - \langle \mathcal{D}_\eta G \rangle_{D_{i,j}^{\mathrm{n}}} \big|_{t_n + \frac{\Delta t}{2}} \Delta t - \langle \widetilde{u}_{i,j+1}^n \rangle_{D_{i,j+1}^{\mathrm{s}}} + \langle \mathcal{D}_\eta G \rangle_{D_{i,j+1}^{\mathrm{s}}} \big|_{t_n + \frac{\Delta t}{2}} \Delta t \Big) \Bigg\} + \mathcal{O}(\Delta t^2). \tag{2.23}
$$

Utilising (2.14) and (2.15) it is straightforward to prove that the contribution of all terms inside the curly brackets is of order Δt. Therefore one can divide the whole equation by Δt and compute the limit $\Delta t \to 0$. For convenience we define the time-dependent numerical fluxes across the cell boundaries

$$
\mathcal{F}_{i+\frac{1}{2}} = \frac{1}{a_{i+\frac{1}{2},j}^+ - a_{i+\frac{1}{2},j}^-} \int_{\eta_{j-\frac{1}{2}}}^{\eta_{j+\frac{1}{2}}} \Big\{ \big(a_{i+\frac{1}{2},j}^+ F(\widetilde{u}_{i,j}) - a_{i+\frac{1}{2},j}^- F(\widetilde{u}_{i+1,j}) \big) - a_{i+\frac{1}{2},j}^+ a_{i+\frac{1}{2},j}^- (\widetilde{u}_{i,j} - \widetilde{u}_{i+1,j}) \Big\} h_\eta h_\phi \, \mathrm{d}\eta \bigg|_{\xi_{i+\frac{1}{2}}}, \tag{2.24}
$$

$$
\mathcal{G}_{j+\frac{1}{2}} = \frac{1}{b_{i,j+\frac{1}{2}}^+ - b_{i,j+\frac{1}{2}}^-} \int_{\xi_{i-\frac{1}{2}}}^{\xi_{i+\frac{1}{2}}} \Big\{ \big(b_{i,j+\frac{1}{2}}^+ G(\widetilde{u}_{i,j}) - b_{i,j+\frac{1}{2}}^- G(\widetilde{u}_{i,j+1}) \big) - b_{i,j+\frac{1}{2}}^+ b_{i,j+\frac{1}{2}}^- (\widetilde{u}_{i,j} - \widetilde{u}_{i,j+1}) \Big\} h_\xi h_\phi \, \mathrm{d}\xi \bigg|_{\eta_{j+\frac{1}{2}}}. \tag{2.25}
$$

at the eastern edge and northern edge, respectively. Using (2.14), (2.15), (2.17) and similar equations for other boundaries one derives the limits of all terms within the curly brackets in (2.23)

$$
\pm \mathcal{F}_{i\pm\frac{1}{2}} \mp \int_{\eta_{j-\frac{1}{2}}}^{\eta_{j+\frac{1}{2}}} h_\eta h_\phi F \, \mathrm{d}\eta \bigg|_{\xi_{i\pm\frac{1}{2}}}
$$

$$
= \lim_{\Delta t \to 0} \frac{\Delta V_{i,j}^{\mathrm{e(w)}} \Delta V_{i\pm1,j}^{\mathrm{w(e)}}}{\Delta V_{i\pm\frac{1}{2},j}} \left(\frac{1}{\Delta t} \langle \widetilde{u}_{i,j}^n \rangle_{D_{i,j}^{\mathrm{e(w)}}} - \langle \mathcal{D}_\xi F \rangle_{D_{i,j}^{\mathrm{e(w)}}} \big|_{t_n + \frac{\Delta t}{2}} - \frac{1}{\Delta t} \langle \widetilde{u}_{i\pm1,j}^n \rangle_{D_{i\pm1,j}^{\mathrm{w(e)}}} + \langle \mathcal{D}_\xi F \rangle_{D_{i\pm1,j}^{\mathrm{w(e)}}} \big|_{t_n + \frac{\Delta t}{2}} \right),
$$

$$
\pm \mathcal{G}_{j\pm\frac{1}{2}} \mp \int_{\xi_{i-\frac{1}{2}}}^{\xi_{i+\frac{1}{2}}} h_\xi h_\phi G \, \mathrm{d}\xi \bigg|_{\eta_{j\pm\frac{1}{2}}}
$$

$$
= \lim_{\Delta t \to 0} \frac{\Delta V_{i,j}^{\mathrm{n(s)}} \Delta V_{i,j\pm1}^{\mathrm{s(n)}}}{\Delta V_{i,j\pm\frac{1}{2}}} \left(\frac{1}{\Delta t} \langle \widetilde{u}_{i,j}^n \rangle_{D_{i,j}^{\mathrm{n(s)}}} - \langle \mathcal{D}_\eta G \rangle_{D_{i,j}^{\mathrm{n(s)}}} \big|_{t_n + \frac{\Delta t}{2}} - \frac{1}{\Delta t} \langle \widetilde{u}_{i,j\pm1}^n \rangle_{D_{i,j\pm1}^{\mathrm{s(n)}}} + \langle \mathcal{D}_\eta G \rangle_{D_{i,j\pm1}^{\mathrm{s(n)}}} \big|_{t_n + \frac{\Delta t}{2}} \right).
$$

The remaining integrals on the left-hand side of these equations cancel out with the cell mean values of flux derivatives in (2.23). Finally we reach the semi-discrete update formula for the volume averaged conservative variables within region $D_{i,j}$

$$
\lim_{\Delta t \to 0} \frac{u_{i,j}^{n+1} - u_{i,j}^n}{\Delta t} = \frac{\mathrm{d} u_{i,j}}{\mathrm{d} t} = - \frac{\mathcal{F}_{i+\frac{1}{2}} - \mathcal{F}_{i-\frac{1}{2}}}{\Delta V_{i,j}} - \frac{\mathcal{G}_{j+\frac{1}{2}} - \mathcal{G}_{j-\frac{1}{2}}}{\Delta V_{i,j}} + \langle S \rangle_{D_{i,j}} \tag{2.26}
$$

with numerical flux functions given by (2.24) and (2.25). Cell mean values of source terms S and volume elements $\Delta V_{i,j}$ should be obtained by integration over the domain $D_{i,j}$ according to (1.9) and (1.10).

Compared to the semi-discrete equation for time-evolution derived in [1] our result offers a higher degree of generality in two ways:

(1) The scheme applies to orthogonal coordinate systems and therefore accounts for area and volume changes of grid zones.
(2) It utilises integral representations for the numerical fluxes instead of approximations with quadrature rules.

The latter point allows us to discretise the numerical fluxes and source terms in different ways starting from the same integral formulas.

2.2. Numerical approximations of flux and source term integrals

The accuracy of the numerical scheme described in the previous section is limited by the order of the polynomials in the reconstruction process. Hence using quadrature rules of higher order to approximate the flux and source term integrals do not improve the overall accuracy of the scheme. Whereas quadrature rules of lower order would compromise the second order accuracy of the scheme and lead to a larger numerical dissipation. Therefore we will consider only second order quadrature schemes.

We carried out the computations for the midpoint and the trapezoidal rule, respectively. From a theoretical point of view both methods differ because the trapezoidal fluxes mix the spatial directions thus leading to a genuinely multidimensional scheme. The midpoint fluxes by contrast can also be obtained via dimensional splitting (cf. remarks in [1]). Since there is almost no difference between the two methods regarding the numerical results we will focus on the midpoint rule in this work. Furthermore we found that the scheme utilising the midpoint rule is more robust in the high Mach number regime. In simulations with remarkably high supersonic flows (Mach number $\gtrsim 100$) we observe that the trapezoidal scheme tends to steepen pressure gradients which may generate negative pressure. Another advantage of the midpoint fluxes over the trapezoidal fluxes is the complexity of the numerical computations which is higher in the latter case.

If we apply the midpoint quadrature rule to the flux integrals (Eqs. (2.24), (2.25)) we have to compute the reconstructed values at the cell interfaces. Hence we define

$$u_{i,j}^{\mathrm{w}} = \widetilde{u}_{i,j}(\xi_{i-\frac{1}{2}}, \eta_j), \qquad u_{i,j}^{\mathrm{s}} = \widetilde{u}_{i,j}(\xi_i, \eta_{j-\frac{1}{2}}), \qquad u_{i,j}^{\mathrm{e}} = \widetilde{u}_{i,j}(\xi_{i+\frac{1}{2}}, \eta_j), \qquad u_{i,j}^{\mathrm{n}} = \widetilde{u}_{i,j}(\xi_i, \eta_{j+\frac{1}{2}}), \tag{2.27}$$

and the numerical fluxes are given by

$$\mathcal{F}_{i+\frac{1}{2}}^{\mathrm{mr}} = \frac{\Delta A_{i+\frac{1}{2},j}}{a_{i+\frac{1}{2},j}^+ - a_{i+\frac{1}{2},j}^-} \left\{ a_{i+\frac{1}{2},j}^+ F(u_{i,j}^{\mathrm{e}}) - a_{i+\frac{1}{2},j}^- F(u_{i+1,j}^{\mathrm{w}}) - a_{i+\frac{1}{2},j}^+ a_{i+\frac{1}{2},j}^- (u_{i,j}^{\mathrm{e}} - u_{i+1,j}^{\mathrm{w}}) \right\}, \tag{2.28}$$

$$\mathcal{G}_{j+\frac{1}{2}}^{\mathrm{mr}} = \frac{\Delta A_{i,j+\frac{1}{2}}}{b_{j+\frac{1}{2},j}^+ - b_{j+\frac{1}{2},j}^-} \left\{ b_{j+\frac{1}{2},j}^+ G(u_{i,j}^{\mathrm{n}}) - b_{j+\frac{1}{2},j}^- G(u_{i,j+1}^{\mathrm{s}}) - b_{j+\frac{1}{2},j}^+ b_{j+\frac{1}{2},j}^- (u_{i,j}^{\mathrm{n}} - u_{i,j+1}^{\mathrm{s}}) \right\}, \tag{2.29}$$

with area elements being

$$\Delta A_{i+\frac{1}{2},j} = h_\eta h_\phi|_{\xi_{i+\frac{1}{2}}, \eta_j} \Delta\eta, \qquad \Delta A_{i,j+\frac{1}{2}} = h_\xi h_\phi|_{\xi_i, \eta_{j+\frac{1}{2}}} \Delta\xi. \tag{2.30}$$

The same rule applied to volume elements and source terms yields

$$\Delta V_{i,j}^{\mathrm{mr}} = h_\xi h_\eta h_\phi|_{\xi_i, \eta_j} \Delta\xi \Delta\eta, \tag{2.31}$$

$$\langle S \rangle_{D_{i,j}}^{\mathrm{mr}} = \frac{1}{\Delta V_{i,j}^{\mathrm{mr}}} S(t, \xi_i, \eta_j) h_\xi h_\eta h_\phi|_{\xi_i, \eta_j} \Delta\xi \Delta\eta = S(t, \xi_i, \eta_j). \tag{2.32}$$

In the cartesian limit all scale factors are identical to one and these formulas reduce to those derived in [1].

If the conservation law under consideration has a vectorial form, inertial forces appear in the curvilinear description (cf. Eq. (1.5)). To account for these geometrical source terms we introduced the concept of commutator coefficients in Section 1.1. These non-linear functions depend on the scale factors h_ξ, h_η, h_ϕ and their derivatives with respect to the coordinates. Numerical approximations of the commutator coefficients may in principle involve Eq. (2.32). The remaining question is, how to approximate the derivatives of the scale factors.

To get a deeper insight into the problem, consider the stationary solutions of the vectorial conservation law (1.1) for the simple tensor field $T(w) = \mathbb{I}_3 \Psi(w)$. $\mathbb{I}_3$ denotes the three-dimensional unit matrix and $\Psi(w)$ is an arbitrary scalar field depending on conservative variables w. Written in orthogonal curvilinear coordinates the stationary solutions require that (see Eqs. (1.5), (1.6))

$$\mathcal{D}_\xi \Psi = (c_{\hat{\eta}\hat{\xi}\hat{\eta}} + c_{\hat{\phi}\hat{\xi}\hat{\phi}})\Psi, \qquad \mathcal{D}_\eta \Psi = (c_{\hat{\xi}\hat{\eta}\hat{\xi}} + c_{\hat{\phi}\hat{\eta}\hat{\phi}})\Psi \tag{2.33}$$

which is clearly equivalent to (see Eq. (A.7))

$$\frac{\partial \Psi}{\partial \xi} = 0, \qquad \frac{\partial \Psi}{\partial \eta} = 0, \tag{2.34}$$

i.e. Ψ is constant. The equations in (2.33) form a system of balance laws rather than a system of conservation laws. It is of particular importance that the numerical scheme is capable of reproducing the correct solution (2.34), e.g. in case of compressible gas dynamics this is the limit of hydrostatic equilibrium. There is an ongoing discussion on the subject addressed by the term of well-balanced schemes (see [14,15]). We will follow a rather simple approach here by analysing the discrete formulation of (2.33) according to the curvilinear central-upwind scheme. Within region D_{ij} the discretised balance laws are given by

$$\frac{\mathcal{F}_{i+\frac{1}{2}}^{\mathrm{mr}} - \mathcal{F}_{i-\frac{1}{2}}^{\mathrm{mr}}}{\Delta V_{i,j}} = \langle (c_{\hat{\eta}\hat{\xi}\hat{\eta}}^{\mathrm{mr}} + c_{\hat{\phi}\hat{\xi}\hat{\phi}}^{\mathrm{mr}})\Psi \rangle_{D_{ij}}, \qquad \frac{\mathcal{G}_{j+\frac{1}{2}}^{\mathrm{mr}} - \mathcal{G}_{j-\frac{1}{2}}^{\mathrm{mr}}}{\Delta V_{i,j}} = \langle (c_{\hat{\xi}\hat{\eta}\hat{\xi}}^{\mathrm{mr}} + c_{\hat{\phi}\hat{\eta}\hat{\phi}}^{\mathrm{mr}})\Psi \rangle_{D_{ij}}.$$

If we apply the midpoint rule to the fluxes (2.28), (2.29) and source terms (2.32), respectively and bear in mind that Ψ is constant we conclude that

$$\frac{\Delta\eta}{\Delta V_{ij}^{\mathrm{mr}}} \left\{ (h_\eta^{\mathrm{e}} h_\phi^{\mathrm{e}} - h_\eta^{\mathrm{w}} h_\phi^{\mathrm{w}}) - \Delta\xi \frac{\partial}{\partial\xi}(h_\eta h_\phi)|_{\xi_i, \eta_j} \right\} = 0, \qquad \frac{\Delta\xi}{\Delta V_{ij}^{\mathrm{mr}}} \left\{ (h_\xi^{\mathrm{s}} h_\phi^{\mathrm{s}} - h_\xi^{\mathrm{n}} h_\phi^{\mathrm{n}}) - \Delta\eta \frac{\partial}{\partial\eta}(h_\xi h_\phi)|_{\xi_i, \eta_j} \right\} = 0 \tag{2.35}$$

should hold. Hence the contribution due to flux differences inside the curly brackets (left) should cancel out the inertial forces (right). This constraint is fulfilled exactly by the choice

$$c^{\mathrm{mr}}_{\hat{\eta}\hat{\xi}\hat{\eta}} = \frac{\Delta\eta}{\Delta V^{\mathrm{mr}}_{i,j}} \frac{h^{\mathrm{e}}_{\phi} + h^{\mathrm{w}}_{\phi}}{2} \left(h^{\mathrm{e}}_{\eta} - h^{\mathrm{w}}_{\eta}\right), \qquad c^{\mathrm{mr}}_{\hat{\xi}\hat{\eta}\hat{\xi}} = \frac{\Delta\xi}{\Delta V^{\mathrm{mr}}_{i,j}} \frac{h^{\mathrm{n}}_{\phi} + h^{\mathrm{s}}_{\phi}}{2} \left(h^{\mathrm{n}}_{\xi} - h^{\mathrm{s}}_{\xi}\right),$$

$$c^{\mathrm{mr}}_{\hat{\phi}\hat{\xi}\hat{\phi}} = \frac{\Delta\eta}{\Delta V^{\mathrm{mr}}_{i,j}} \frac{h^{\mathrm{e}}_{\eta} + h^{\mathrm{w}}_{\eta}}{2} \left(h^{\mathrm{e}}_{\phi} - h^{\mathrm{w}}_{\phi}\right), \qquad c^{\mathrm{mr}}_{\hat{\phi}\hat{\eta}\hat{\phi}} = \frac{\Delta\xi}{\Delta V^{\mathrm{mr}}_{i,j}} \frac{h^{\mathrm{n}}_{\xi} + h^{\mathrm{s}}_{\xi}}{2} \left(h^{\mathrm{n}}_{\phi} - h^{\mathrm{s}}_{\phi}\right) \tag{2.36}$$

for the midpoint rule commutator coefficients.

3. Numerical experiments

In the numerical examples we focus on the Euler equations for inviscid compressible and non-heat-conducting gas dynamics. This system of non-linear conservation laws may be written in generalised orthogonal coordinates according to (1.7). Thereby we assumed symmetry of the flow with respect to the spatial coordinate ϕ. The vectors of conservative variables and fluxes in the ξ and η directions are given by

$$u = \begin{bmatrix} \varrho \\ \varrho v_{\hat{\xi}} \\ \varrho v_{\hat{\eta}} \\ \varrho v_{\hat{\phi}} \\ E \end{bmatrix}, \qquad F = \begin{bmatrix} \varrho v_{\hat{\xi}} \\ \varrho v^2_{\hat{\xi}} + p \\ \varrho v_{\hat{\xi}} v_{\hat{\eta}} \\ \varrho v_{\hat{\xi}} v_{\hat{\phi}} \\ (E+p) v_{\hat{\xi}} \end{bmatrix}, \qquad G = \begin{bmatrix} \varrho v_{\hat{\eta}} \\ \varrho v_{\hat{\eta}} v_{\hat{\xi}} \\ \varrho v^2_{\hat{\eta}} + p \\ \varrho v_{\hat{\eta}} v_{\hat{\phi}} \\ (E+p) v_{\hat{\eta}} \end{bmatrix}. \tag{3.1}$$

If we furthermore assume, that the equation of state is determined by the ideal gas equation, the total energy E depends on the density ϱ, the pressure p as well as the velocity components $v_{\hat{\xi}}$, $v_{\hat{\eta}}$ and $v_{\hat{\phi}}$, respectively

$$E = \frac{1}{2}\varrho\left(v^2_{\hat{\xi}} + v^2_{\hat{\eta}} + v^2_{\hat{\phi}}\right) + \frac{p}{\gamma - 1}. \tag{3.2}$$

Here γ denotes the constant ratio of specific heats. It is set to $\gamma = 1.4$ in all test configurations. For the geometrical source terms one computes with the commutator coefficients (A.7)

$$S = \varrho v_{\hat{\xi}} \begin{bmatrix} 0 \\ -v_{\hat{\eta}} c_{\hat{\xi}\hat{\eta}\hat{\xi}} \\ v_{\hat{\xi}} c_{\hat{\xi}\hat{\eta}\hat{\xi}} \\ -v_{\hat{\phi}} c_{\hat{\phi}\hat{\xi}\hat{\phi}} \\ 0 \end{bmatrix} + \varrho v_{\hat{\eta}} \begin{bmatrix} 0 \\ v_{\hat{\eta}} c_{\hat{\eta}\hat{\xi}\hat{\eta}} \\ -v_{\hat{\xi}} c_{\hat{\eta}\hat{\xi}\hat{\eta}} \\ -v_{\hat{\phi}} c_{\hat{\phi}\hat{\eta}\hat{\phi}} \\ 0 \end{bmatrix} + \varrho v^2_{\hat{\phi}} \begin{bmatrix} 0 \\ c_{\hat{\phi}\hat{\xi}\hat{\phi}} \\ c_{\hat{\phi}\hat{\eta}\hat{\phi}} \\ 0 \\ 0 \end{bmatrix} + p \begin{bmatrix} 0 \\ c_{\hat{\eta}\hat{\xi}\hat{\eta}} + c_{\hat{\phi}\hat{\xi}\hat{\phi}} \\ c_{\hat{\xi}\hat{\eta}\hat{\xi}} + c_{\hat{\phi}\hat{\eta}\hat{\phi}} \\ 0 \\ 0 \end{bmatrix}. \tag{3.3}$$

Besides these geometrical sources we do not account for additional body forces. Therefore all units can be removed from the system given above. In all tests we use this dimensionless prescription of the equations of gas dynamics. In Sections 3.1 and 3.2 we examine Riemann problems with the initial data of $v_{\hat{\phi}}$ set to zero. In this case $v_{\hat{\phi}}$ remains zero and the fourth component of the vectors in (3.1) and (3.3) vanishes. The system of Euler equations reduces to a pure two-dimensional problem without any flow in the direction of ϕ. In Section 3.3 we study three-dimensional flows with rotational symmetry. The fourth equation of the above mentioned system then describes the conservation of the angular momentum.

To advance the numerical solution in time according to (2.26) we used a third order Runge–Kutta scheme as described in [16,17]. Cell boundary data is obtained via piecewise linear reconstruction. Unless stated otherwise we apply the *monotonised-central* limiter proposed in [18]

$$\mathrm{mc}(\Delta_{i-\frac{1}{2},j}, \Delta_{i+\frac{1}{2},j}, \Delta_{i,j}) = \mathrm{minmod}(\theta\Delta_{i-\frac{1}{2},j}, \Delta_{i,j}, \theta\Delta_{i+\frac{1}{2},j}) \tag{3.4}$$

with parameter $\theta \in [1, 2]$. The left-handed, right-handed and central differences – e.g. in the ξ-directions – are given by

$$\Delta_{i-\frac{1}{2},j} = \frac{u_{i,j} - u_{i-\frac{1}{2},j}}{\Delta\xi}, \qquad \Delta_{i+\frac{1}{2},j} = \frac{u_{i+\frac{1}{2},j} - u_{i,j}}{\Delta\xi}, \qquad \Delta_{i,j} = \frac{u_{i+\frac{1}{2},j} - u_{i-\frac{1}{2},j}}{2\Delta\xi},$$

and the multivariable minmod function is evaluated according to

$$\mathrm{minmod}(x_1, \ldots, x_n) = \begin{cases} \min(x_1, \ldots, x_n) & \text{if } x_i > 0 \; \forall i, \\ \max(x_1, \ldots, x_n) & \text{if } x_i < 0 \; \forall i, \\ 0 & \text{otherwise.} \end{cases} \tag{3.5}$$

The amount of numerical diffusion is controlled by the parameter θ. Lower values are more diffusive while higher values result in an unstable scheme. In most of the test problems we set the parameter $\theta = 1.3$. This is less diffusive than the ordinary minmod limiter (which corresponds to $\theta = 1.0$) but retains stability in most cases.

In this work we present only the results obtained for the numerical scheme utilising the midpoint rule. However, we performed the same simulations for the trapezoidal fluxes as well. We found that the differences of the numerical solutions are negligible.
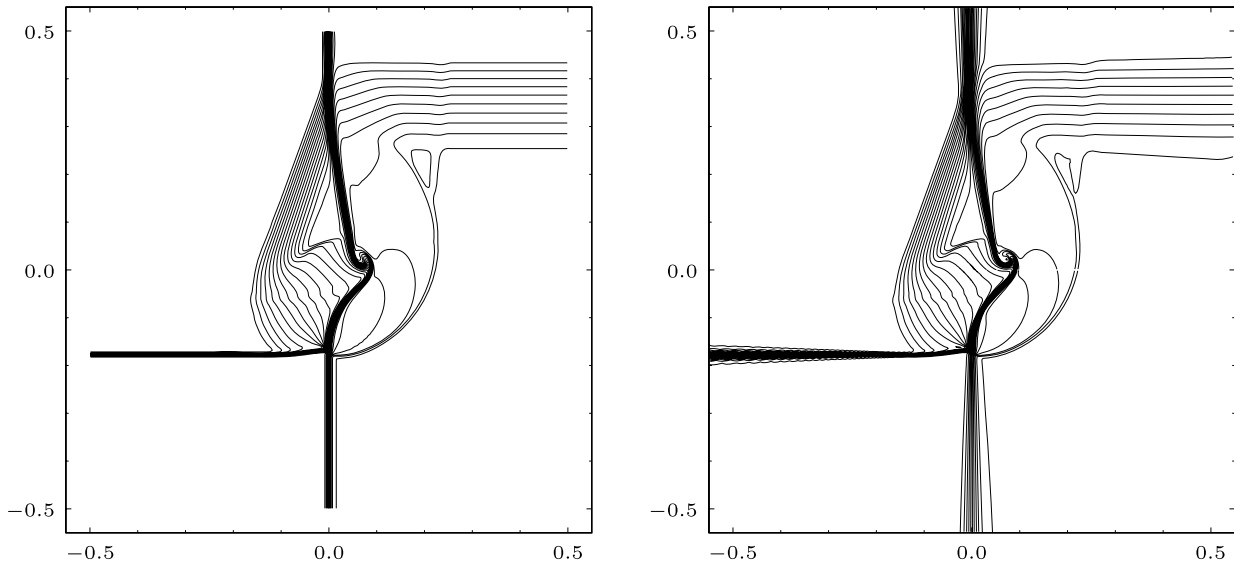
Fig. 3.1. Density at time $t = 0.2$ computed on a cartesian mesh (left) and polar mesh (right) using midpoint rule for flux calculations. 30 equally spaced contour levels between 0.525 and 2.025.

3.1. Two-dimensional Riemann problem on a polar mesh

In this section we analyse the numerical solutions of two-dimensional Riemann problems on a polar mesh. The same tests were used by Kurganov and Tadmor [1] for comparison with the numerical results of Schulz-Rinne et al. [19] as well as Lax and Liu [20]. The computational domain is a square in the cartesian case and a circle for the polar mesh with the origin in the centre in both cases. At time $t = 0$ the simulation is initialised with piecewise constant data in the quadrants defined by the x- and y-axis.

Kurganov and Tadmor studied the numerical solutions of 19 different configurations. Since our numerical schemes differ only from those described in [1] by means of the geometrical factors, we will focus on the discrepancies due to the polar mesh. Differences between computations on cartesian and polar grids would appear in each of the 19 test cases. Therefore we show only our results obtained for test configuration number 18 in [1] with the initial data

$$
\begin{aligned}
&p_2 = 1, &&\varrho_2 = 2, &&p_1 = 1, &&\varrho_1 = 1, \\
&u_2 = 0, &&v_2 = -0.3, &&u_1 = 0, &&v_1 = 1, \\
\\
&p_3 = 0.4, &&\varrho_3 = 1.0625, &&p_4 = 0.4, &&\varrho_4 = 0.5197, \\
&u_3 = 0, &&v_3 = 0.2145, &&u_4 = 0, &&v_4 = 0.2741.
\end{aligned}
$$

u and v denote the velocity in the x- and y-direction, respectively. The north-eastern quadrant has index 1, the others are labelled counterclockwise in ascending order. These initial conditions generate a shock-wave between quadrants 2 and 3, a rarefaction-wave between quadrants 1 and 4 and contact discontinuities between quadrants 1 and 2 as well as 3 and 4. In the centre of the computational domain the 4 different solutions join leading to a complex flow.

The system of equations under consideration is given by (3.1), (3.2) and (3.3) with $v_{\hat{\phi}}$ set to zero. For cartesian coordinates all scale factors are unity and the commutator coefficients and thus all geometrical source terms vanish. In case of the polar grid we identify $\xi = r$, $\eta = \varphi$, $\phi = z$, respectively and assume slab symmetry, i.e. all derivatives with respect to z are zero. The scale factors are $h_r = 1$, $h_\varphi = r$ and $h_z = 1$. The remaining non-vanishing commutator coefficient is therefore

$$
c_{\hat{\eta}\hat{\xi}\hat{\eta}} \equiv c_{\varphi r \varphi} = \frac{1}{h_r h_\varphi} \frac{\partial h_\varphi}{\partial r} = \frac{1}{r}.
$$

The computational domain covers a region of 1×1 in non-dimensional units with a resolution of 400×400 cells on the cartesian mesh. In case of the polar coordinates the extent of the circular domain is so large, that the unit square fits exactly into it. Thus the radius of the computational domain is $\sqrt{2}/2$ with a resolution of 282 cells. The angular resolution is 360 for the full 2π circular domain. The parameter for the limiter was set to $\theta = 1.3$ in all examples and the Courant number is 0.4. A stability criterion (CFL condition) similar to that proposed by Courant, Friedrichs and Lewy [21] for an explicit central-upwind scheme is given in [3].

Fig. 3.1 shows the density contours for this two-dimensional Riemann problem. The results given in [1] for cartesian geometry are similar to ours besides the small 'bump' in the north-western quadrant. This structure shows only up in our results if we insert an intermediate contour level at $\varrho = 2.0125$. Unfortunately the absolute scale of the contour levels is not given in [1]. Since the 'bump' is also not present in the results of Lax and Liu [20] we cannot exclude it being an artefact probably caused by the plotting routine.

In the simulations on the polar mesh we achieved results which are almost identical to the cartesian case. The small deviations are due to the fact that the angular resolution of the polar scheme decreases with increasing distance to the centre. Therefore at a distance of 0.2 from the centre the shocks and contacts are less sharp on the polar mesh and they tend to fan out towards the boundaries. The same applies to the rarefactions in the north-eastern quadrant. On the other hand a close inspection of the results reveals that the polar scheme benefits from the higher angular resolution near the origin. The shocks and other features there are resolved slightly better.
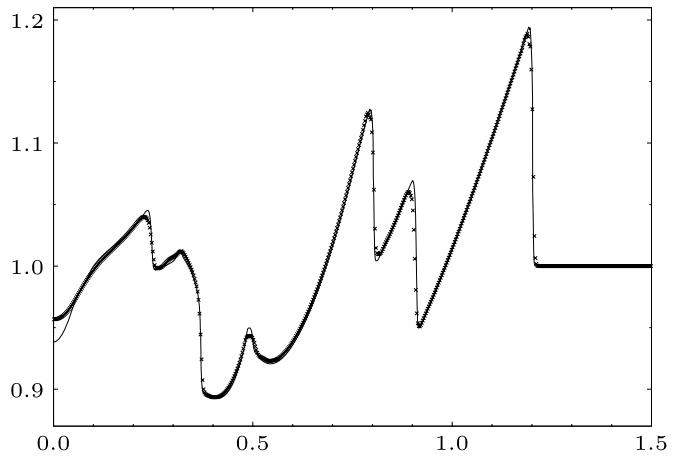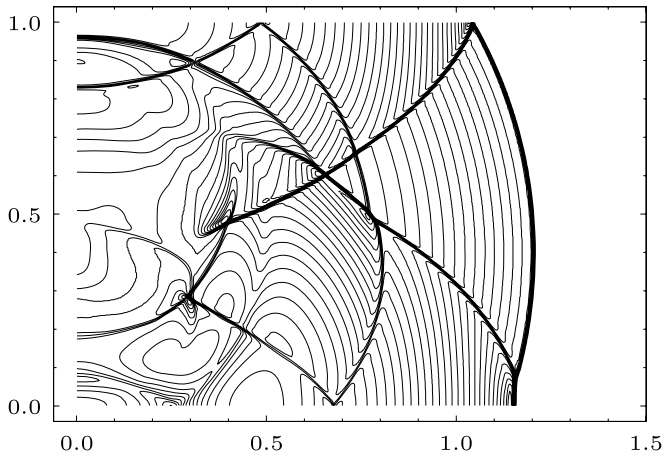
Fig. 3.2. Pressure in the r–z-plane at time $t = 0.7$. 32 equally spaced contour levels between 0.73 and 1.48.

Fig. 3.3. Horizontal profile of the pressure at $z = 0.4$ and time $t = 0.7$. The continuous line shows the result for doubled resolution.

3.2. Spherical Riemann problem between walls on a cylindrical mesh

Langseth and LeVeque proposed a spherical Riemann problem in [22]. The flow under investigation is rotationally symmetric and may be examined using cylindrical coordinates. Therefore we identify $\xi = z$, $\eta = r$, $\phi = \varphi$ and assume symmetry with respect to the polar angle φ. The geometrical scale factors are given by $h_z = 1$, $h_r = 1$ and $h_\varphi = r$. In this case the only non-vanishing commutator coefficient is

$$c_{\hat{\phi}\hat{\eta}\hat{\phi}} \equiv c_{\varphi r \varphi} = \frac{1}{h_\varphi h_r} \frac{\partial h_\varphi}{\partial r} = \frac{1}{r}.$$

The initial condition is a homogeneous density distribution $\varrho_0 = 1$ with vanishing velocities. Inside a sphere with a radius of $r = 0.2$ centred at $z = 0.4$ the pressure is set to 5 and outside to 1. The fourth equation can be removed from the system given by (3.1), (3.2) and (3.3), because initially there is no angular motion. Hence v_φ remains zero. The computational domain covers a region of $[0, 1.0] \times [0, 1.5]$ in the r–z-plane with a resolution of 400×600 cells. The parameter for the *monotonised-central* limiter is set to $\theta = 1.3$ and the Courant number is 0.4 in all computations.

In Fig. 3.2 the pressure at time $t = 0.7$ in the r–z-plane is shown for the central-upwind scheme with midpoint rule fluxes. The positions of the shocks are identical to those computed in [22]. There are small deviations from their solutions in the central region along the axis. In this domain the flow becomes stationary with low mass density. This discrepancy becomes more obvious in the pressure profiles shown in Fig. 3.3. The solid line in this diagram corresponds to a solution obtained on a finer grid with a resolution of 800×1200 cells. In the limit $r \to 0$ the pressure on the coarse grid is a little above 0.95, but the solution converges to the value stated in [22] as the grid is refined.

3.3. Detailed conservation of angular momentum

The test introduced in this section makes use of an important property of inviscid rotationally symmetric flows: The coupling of angular momentum transport to mass transport. If one defines the *specific angular momentum* by

$$\ell = h_\phi v_{\hat{\phi}} \tag{3.6}$$

the fourth component of the system (1.7) with (3.1), (3.3) may be rewritten in the form

$$\partial_t (\varrho \ell) + \mathcal{D}_\xi (\varrho \ell v_{\hat{\xi}}) + \mathcal{D}_\eta (\varrho \ell v_{\hat{\eta}}) = 0. \tag{3.7}$$

This equation describes the advection of angular momentum density $\varrho \ell$ in curvilinear orthogonal coordinates with rotational symmetry. It is of the very same form as the equation for transport of mass density ϱ, i.e. the continuity equation

$$\partial_t \varrho + \mathcal{D}_\xi (\varrho v_{\hat{\xi}}) + \mathcal{D}_\eta (\varrho v_{\hat{\eta}}) = 0. \tag{3.8}$$

The time evolution of specific angular momentum is hence given by

$$\partial_t \ell = -\frac{v_{\hat{\xi}}}{h_\xi} \partial_\xi \ell - \frac{v_{\hat{\eta}}}{h_\eta} \partial_\eta \ell. \tag{3.9}$$

3.3.1. The mass spectrum as a constant of motion

Following the definition of Norman et al. [23] we define the mass spectrum of the specific angular momentum by

$$M(\ell) = \int_0^\ell dm(\ell') \tag{3.10}$$

with $m(\ell')$ being the mass distribution function with respect to specific angular momentum. For inviscid axisymmetric flows this spectrum is a constant of motion within a spatial region D if there is no flux across its boundary ∂D

$$\left.\frac{\mathrm{d}M}{\mathrm{d}t}\right|_D = 0 \quad \text{if } \hat{n} \cdot v|_{\partial D} = 0. \tag{3.11}$$

$\hat{n}$ is the surface normal of the boundary and v the velocity of the fluid. With the help of the step function we may transform the mass integral in (3.10) into a volume integral

$$\left.\frac{\mathrm{d}M}{\mathrm{d}t}\right|_D = \frac{\mathrm{d}}{\mathrm{d}t} \int_D \Theta\big(\ell - \ell'(\xi, \eta, t)\big)\varrho(\xi, \eta, t)\,\mathrm{d}V(\xi, \eta).$$

The spatial region D does not depend on time, hence it can be exchanged with the time derivative within the integration.

$$\left.\frac{\mathrm{d}M}{\mathrm{d}t}\right|_D = \int_D \partial_t \Theta(\ell - \ell')\varrho\,\mathrm{d}V + \int_D \Theta(\ell - \ell')\partial_t\varrho\,\mathrm{d}V. \tag{3.12}$$

In doing so we implied that the derivative of the step function is well defined (see [24]). Eqs. (3.8) and (3.9) allow us to replace the time derivatives with spatial ones. For convenience we define the two-dimensional restrictions of the usual curvilinear differential operators by

$$\widehat{\nabla} \cdot v = \mathcal{D}_\xi v_{\hat{\xi}} + \mathcal{D}_\eta v_{\hat{\eta}} \quad \text{and} \quad v \cdot \widehat{\nabla}\ell = \frac{v_{\hat{\xi}}}{h_\xi}\partial_\xi\ell + \frac{v_{\hat{\eta}}}{h_\eta}\partial_\eta\ell.$$

Therefore (3.12) becomes

$$\left.\frac{\mathrm{d}M}{\mathrm{d}t}\right|_D = -\int_D \varrho v \cdot \widehat{\nabla}\ell' \frac{\mathrm{d}}{\mathrm{d}\ell'}\Theta(\ell - \ell')\,\mathrm{d}V - \int_D \Theta(\ell - \ell')\widehat{\nabla} \cdot (\varrho v)\,\mathrm{d}V.$$

The second integral may be evaluated by using integration by parts and applying the Gaussian divergence theorem

$$\left.\frac{\mathrm{d}M}{\mathrm{d}t}\right|_D = -\int_D \varrho v \cdot \widehat{\nabla}\Theta(\ell - \ell')\,\mathrm{d}V - \int_{\partial D} \varrho\Theta(\ell - \ell')v \cdot \hat{n}\,\mathrm{d}A + \int_D \varrho v \cdot \widehat{\nabla}\Theta(\ell - \ell')\,\mathrm{d}V = 0.$$

The surface integral yields zero due to the vanishing normal velocity across the boundary.

The mass spectrum $M(\ell)$ – although a global quantity – carries information about the local redistribution of angular momentum. Any kind of diffusive transport of the angular momentum causes a deviation from the initial spectrum. Since numerical diffusion exists in any numerical scheme, we do not expect an exact conservation of the mass spectrum.

3.3.2. Analytical expressions for the mass spectrum

In general the evaluation of the integral in (3.10) is difficult and must be done numerically. However, for a quantitative analysis it is very useful for comparison to start numerical simulations with angular momentum distributions for which analytical expressions of the mass spectrum exist. Since cylindrical coordinates $\{z, r, \varphi\}$ exhibit the natural system for the formulation of rotationally symmetric problems, we will perform all calculations in this system and assume symmetry with respect to φ. Let us define the surface density by

$$\Sigma(r) = \int_{-\infty}^{\infty} \varrho(r, z)\,\mathrm{d}z \tag{3.13}$$

and demand that this function is well defined for $r \in \mathbb{R}^+$. If we claim that the specific angular momentum depends only on r, then the mass spectrum (3.10) may be written in terms of the surface density

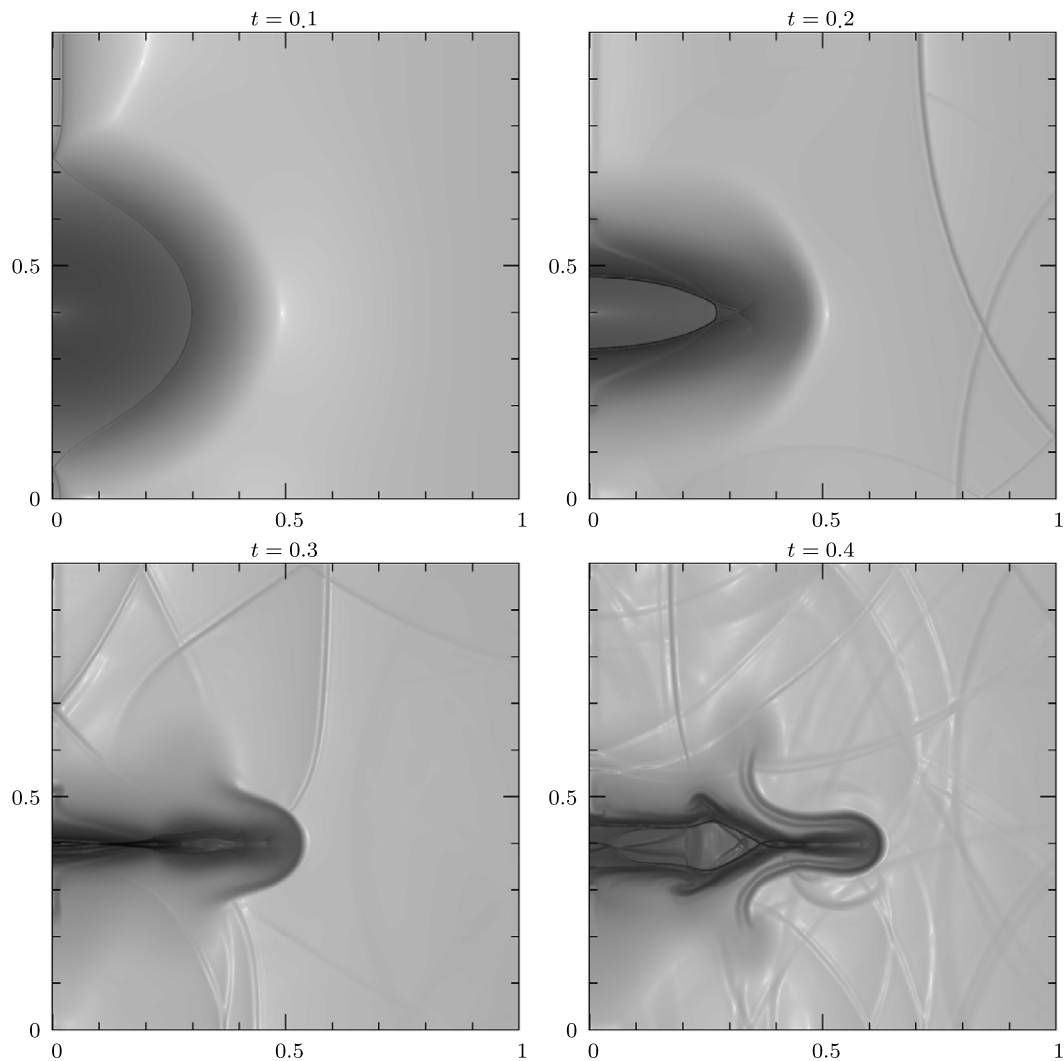$$M(\ell) = 2\pi \int_0^{\infty} \Sigma(r)\Theta\big((\ell - \ell'(r)\big)r\,\mathrm{d}r. \tag{3.14}$$

Let us furthermore assume that $\ell'(r)$ is of the form

$$\ell'(r) = \ell_0 \left(\frac{r}{r_0}\right)^\alpha \quad \text{with } \alpha, \ell_0, r_0 \in \mathbb{R}^+ \tag{3.15}$$

then the inverse function $r(\ell') = r_0(\ell'/\ell_0)^{1/\alpha}$ is well defined and the mass spectrum becomes

$$M(\ell) = 2\pi \int_0^{r(\ell)} \Sigma(r)r\,\mathrm{d}r. \tag{3.16}$$

The last integral may be evaluated analytically in some cases. We will consider mass distributions for which $\Sigma(r)$ is a very simple function of r:

Fig. 3.4. Schlieren type images showing the absolute value of the density gradient at different times; logarithmic scale between 10^{-5} (white) and 10^4 (black). The solution was obtained on a 800×800 cylindrical grid.

(1) homogeneous cylinder centred on the axis with radius R and mass M_0

$$M(\ell) = M_0 \left(\frac{r_0}{R}\right)^2 \left(\frac{\ell}{\ell_0}\right)^{2/\alpha}. \tag{3.17}$$

(2) homogeneous sphere centred on the axis with radius R and mass M_0

$$M(\ell) = M_0 \left[1 - \left(1 - \left(\frac{r_0}{R}\right)^2 \left(\frac{\ell}{\ell_0}\right)^{2/\alpha} \right)^{3/2} \right]. \tag{3.18}$$

(3) Gaussian density distribution centred on the axis with standard deviation σ and mass M_0

$$M(\ell) = M_0 \left[1 - \exp\left(-\frac{1}{2} \left(\frac{r_0}{\sigma}\right)^2 \left(\frac{\ell}{\ell_0}\right)^{2/\alpha} \right) \right]. \tag{3.19}$$

These expressions become even simpler for rigid motion. In this case $\alpha = 2$ and the specific angular momentum may be expressed in terms of the constant angular velocity Ω_0

$$\ell(r) = \frac{\ell_0}{r_0^2} r^2 = \Omega_0 r^2.$$

The spectrum of a rigidly rotating sphere (3.18) then reduces to the formula given in [23].

3.3.3. The rigidly rotating Gaussian density distribution

In this test we examine the disruption of a Gaussian density pulse by centrifugal forces. A dense pulse is located on the axis of symmetry within a low density environment. The rotational velocity in the whole computational domain is initialised with constant
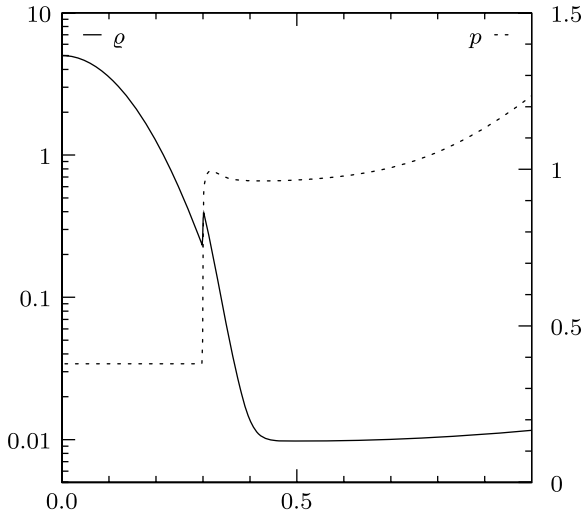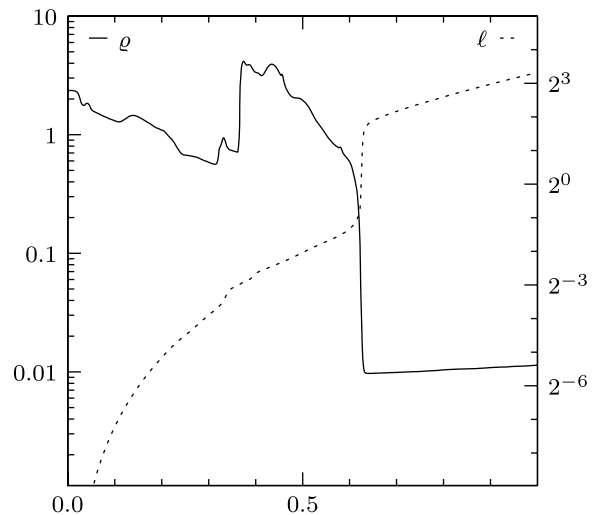
Fig. 3.5. Profile of mass density (solid line, left scale) and pressure (dashed line, right scale) at $z = 0.4$ and time $t = 0.1$.
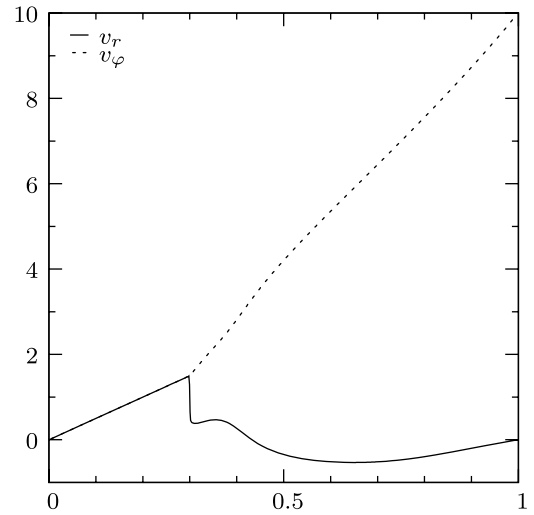
Fig. 3.6. Profile of radial velocity v_r (solid line) and rotational velocity v_φ (dashed line) at $z = 0.4$ and time $t = 0.1$.
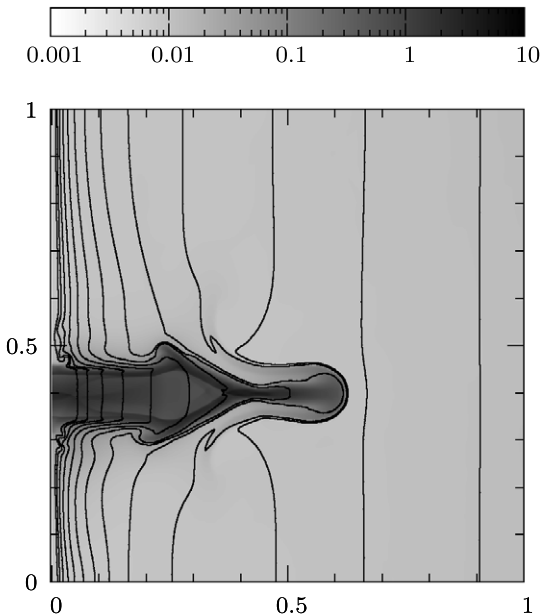
Fig. 3.7. Mass density and specific angular momentum (contours) at time $t = 0.4$. The contour level scale is logarithmic with basis 2 starting at 2^{-9}.


Fig. 3.8. Profile of mass density (solid line, left scale) and specific angular momentum (dashed line, right scale) at $z = 0.4$ and time $t = 0.4$.

angular velocity, i.e. $v_\varphi = \Omega_0 r^2$ with $\Omega_0 = 10$. All other velocity components are set to zero and the pressure is unity. The peak density of the pulse is $\varrho_{max} = 10$ and the uniform density of the ambient medium is $\varrho_{min} = 10^{-2}$. The pulse is centred at $(r, z) = (0, 0.4)$ with a full width half mean of 0.1. On the cylindrical mesh the computational domain covers a region of $[0, 1] \times [0, 1]$ with reflecting boundary conditions at all boundaries. In addition we switched the sign of the rotational velocity within the ghost zones along the axis of symmetry. All computations in this chapter were performed using the midpoint quadrature scheme with the monotonised central limiter and a Courant number of 0.4. The limiters parameter was set to $\theta = 1.3$ unless stated otherwise.

This problem setup ensures that a huge amount of mass with low specific angular momentum spreads out into the whole computational domain. The dynamic behaviour is, at least in the beginning, mostly driven by centrifugal forces. Hence the dynamic time scale is dominated by the time of circulation, which is roughly $1/\Omega_0 = 0.1$. Fig. 3.4 depicts the time evolution of the flow up to $t = 0.4$ for a resolution of 800×800 cells. The forces acting on the density pulse accelerate the gas to supersonic speed in the radial direction forming a bow shock. One clearly sees how the material of the dense region is driven outwards. Within this central region behind the shock the peak density drops to 5.0 at time $t = 0.1$ and the pressure arrives at a constant value of 0.3787 (cf. Fig. 3.5). Since the pressure gradient inside this bubble confined by the shock is zero, there are no forces acting in the vertical direction and v_z remains zero. Furthermore the remarkable identity $v_r = v_\varphi$ holds as can be seen for $z = 0.4$ in Fig. 3.6. At $t = 0.2$ the density pulse has flattened to a disk like structure causing the low pressure region to collapse roughly around $t = 0.3$.

Another interesting feature forms around $(r, z) = (0.5, 0.4)$ which is very much like the well-known Rayleigh–Taylor instability [25,26]. The dense material of the pulse penetrates into the rarefied gas of the ambient medium, in this case driven by centrifugal forces. These instabilities grow rapidly and the flow becomes more and more turbulent from the time $t = 0.4$ (q.v. Fig. 3.12).
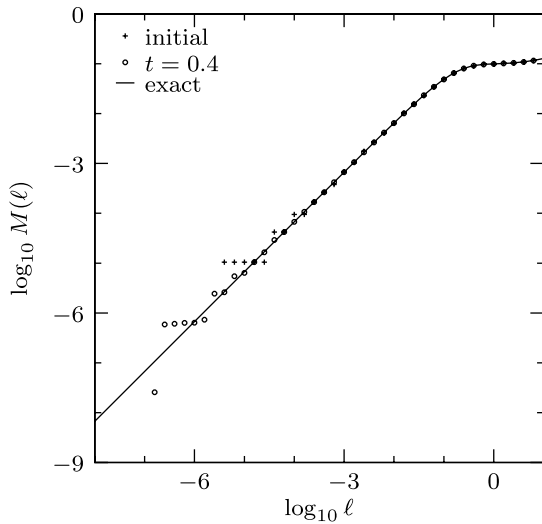
Fig. 3.9. Mass spectrum of specific angular momentum for the initial condition and at time $t = 0.4$; the resolution of the simulation is 800×800.
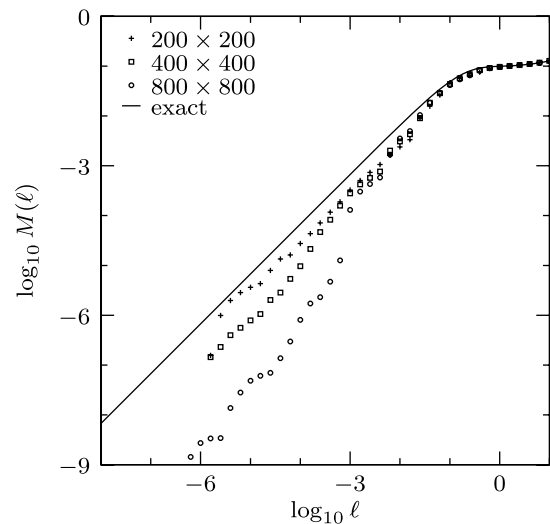
Fig. 3.10. Mass spectrum of specific angular momentum at time $t = 1.0$ for different resolutions.
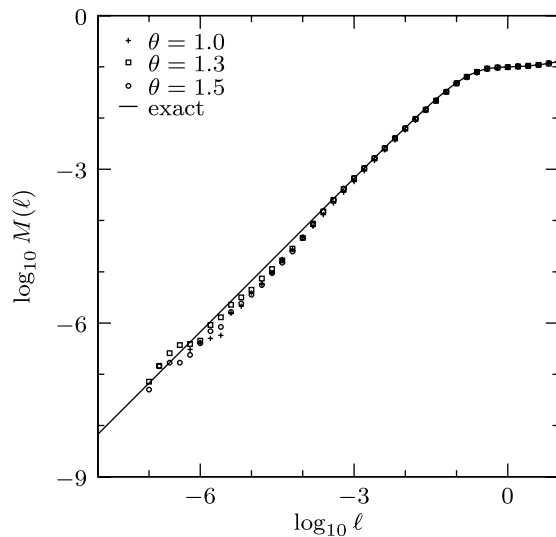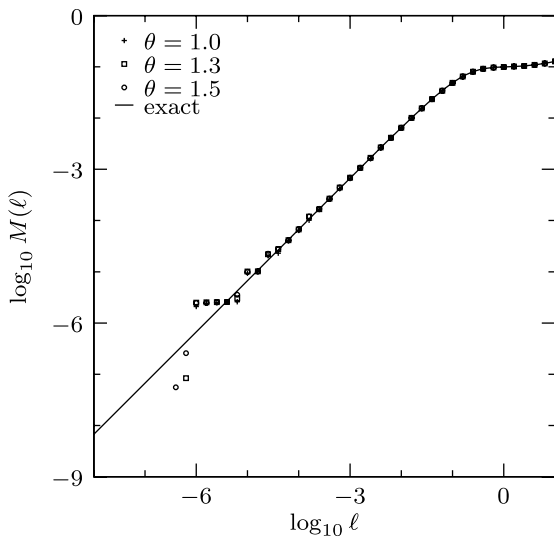

Fig. 3.11. Mass spectrum of specific angular momentum. Comparison of the results for different settings of the monotonised-central limiter at times $t = 0.4$ (left) and $t = 0.6$ (right); the resolution of the simulations is 400×400.

The outwards driven material carries a vast amount of the mass initially concentrated around $(r, z) = (0, 0.4)$. Connected to this mass flux gas with low specific angular momentum is transported to larger radii as can be seen in Figs. 3.7 and 3.8. The question under consideration is whether this redistribution in space is solely advective or partly diffusive. Therefore we compute the mass spectrum as described in the previous sections. In this test problem the exact solution can be obtained via summation of the two solutions for the Gaussian density pulse (Eq. (3.19)) and the homogeneous cylinder (Eq. (3.17)) with different total masses M_0. In Fig. 3.9 this analytical solution is depicted in conjunction with the initial spectrum and the numerical result at time $t = 0.4$. The steep slope in this logarithmic diagram starting at $\ell = 10^{-6}$ indicates the Gaussian pulse whereas the kink at $\ell = 10^{-1}$ marks the transition to the ambient medium. Besides some spurious data points at the lower end of the spectrum, the numerical result is in good agreement with the exact solution. Due to the limited resolution of the numerical computation, there are some data points with different angular momentum attached to the same mass. This shows up in both the initial setup and in the results for $t = 0.4$. Also there is clearly a lower limit for mass and specific angular momentum determined by the size of the grid cells and the distance between the barycentres of the innermost cells and the axis.

The picture becomes completely different, if we examine the data at later times. After the generation of the first instabilities diffusive processes effect the redistribution of angular momentum. This shows up in the loss of cells with low mass causing a steeper slope in the spectrum seen in Fig. 3.10. Even more noteworthy there is a dependence on the resolution, which seems to be contradictory. The simulations with low resolution produce better results, whereas the numerical diffusion should decrease with increasing resolution. To study the influence of the numerical diffusion we changed the parameter of the monotonised-central limiter (see Eq. (3.4)). In general one observes that higher values of θ result in less diffusive schemes. In Fig. 3.11 the mass spectrum before and after the generation of the first instabilities is shown for different settings of the limiter. Up to $t = 0.4$ there is almost no dependence on the limiters parameter θ. At later times diffusive angular momentum transport occurs as in the previous experiment. However, a comparison of the mass spectra is questionable if instabilities are generated. In such a case a proposition regarding the conservation of angular momentum is of limited significance, because the spatial redistribution of angular momentum proceeds differently.
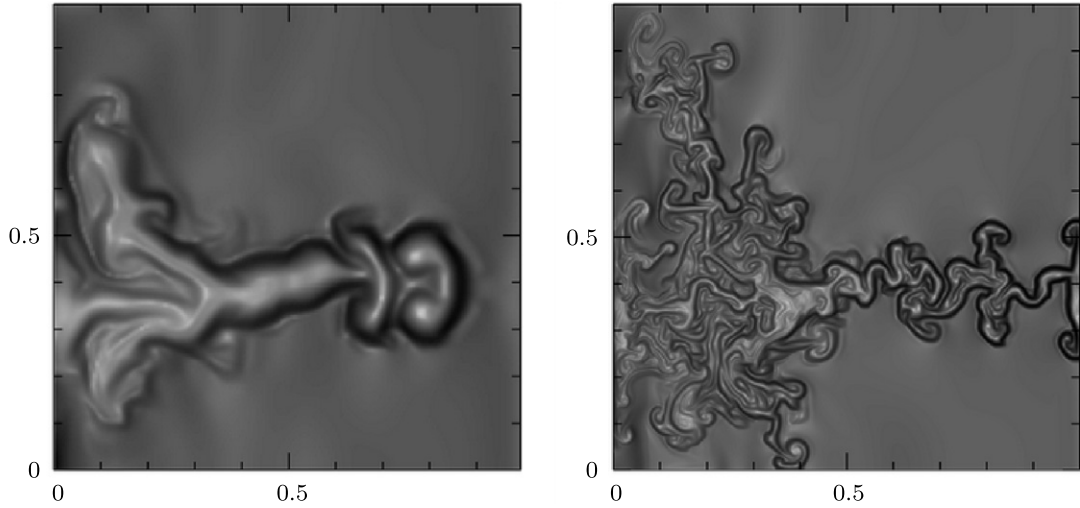
Fig. 3.12. Absolute value of the projection of the vorticity onto the r–z-plane. Comparison of the results for two different resolutions; left image: 200×200, right image 800×800; both at time $t = 1.0$.

To shed light on this phenomenon, we compared the vorticity of the numerical results at the same time for different resolutions. In cylindrical coordinates with rotational symmetry the components of the vorticity are given by

$$w_r = -\frac{\partial v_\varphi}{\partial z}, \qquad w_z = \frac{1}{r}\frac{\partial}{\partial r}(rv_\varphi) \quad \text{and} \quad w_\varphi = \frac{\partial v_r}{\partial z} - \frac{\partial v_z}{\partial r}. \tag{3.20}$$

With help of (3.9) one easily verifies, that

$$\partial_t \ell = r(v_z w_r - v_r w_z) \tag{3.21}$$

holds. Hence there is a close connection between the time evolution of specific angular momentum and the projection of the vorticity onto the r–z-plane. Fig. 3.12 shows the absolute value of the projected vorticity for simulations performed with different resolutions. It is quite obvious that the resolution has a significant impact on the results. Lower resolution seems to prevent the generation of eddies on small scales, a characteristic property of simulations which exhibit turbulent motion. At first glance one could think that – as far as angular momentum is concerned – the different time-evolution of the simulations should not affect conservation of the mass spectrum. This conclusion is not entirely true since we expect that numerical diffusion prevents exact conservation of the spectrum. Normally the numerical diffusion declines as the grid is refined, but only if the overall solution is not altered significantly. However, this is exactly what happens in case of the angular momentum test as soon as turbulent motion dominates the flow.

Let us recall how the numerical diffusion enters the scheme. The basic idea is that one has to damp spurious oscillations caused by the linear interpolation in the vicinity of discontinuities. To achieve this we introduced non-linear functions which act on the slopes (see Section 2). The diffusive effects due to this mechanism become large in regions with steep gradients. In Fig. 3.12 the dark areas are an indicator for large vorticity therefore marking the regions with steep gradients in specific angular momentum. It is in these areas where the artificial diffusive transport happens. One clearly sees that the high resolution simulation exhibits a lot more of those areas with a steep gradient in vorticity. Thus the impact of numerical diffusion on the angular momentum transport is much higher than in the low resolution simulation.

Finally we compare our numerical scheme to the well-known second-order-accurate van Leer method [4] used in the ZEUS-2D code [27] developed by Stone and Norman [28]. The ZEUS-2D code implements the numerical scheme for consistent angular momentum transport proposed by Norman et al. [23] and improved by Norman and Winkler [29]. The results depicted in Fig. 3.13 were computed with a von Neumann and Richtmyer type scalar artificial viscosity [30]. The parameter which controls the strength was set to 2.0. For comparison we performed the same tests using the tensorial artificial viscosity [31], but the results were almost identical. The mass spectra obtained for these simulations show diffusive transport in the low-mass and low-angular-momentum regime. We found that the ZEUS-2D code generates grid zones with zero angular momentum indicated by the horizontal branch in the left diagram of Fig. 3.13. This leads to an overestimation of the mass confined in grid zones with low specific angular momentum. Henceforth the shape of the mass spectrum changes rapidly, when the first instabilities appear, especially for higher resolution. By contrast, the mass spectrum computed for the new curvilinear central-upwind scheme does not show major deviations from the exact solution for $t \leqslant 0.6$.

3.4. The Gaussian pulse on an oblate spheroidal mesh

The following test is meant as a demonstration for the validity of the numerical scheme applied to other orthogonal and rotationally symmetric coordinate systems. Hence we selected oblate spheroidal coordinates $\{\xi, \eta, \phi\}$ (see e.g. [32], Ch. 21.3) with

$$\begin{pmatrix} x \\ y \\ z \end{pmatrix} = \begin{pmatrix} a\tilde{\xi}\tilde{\eta}\cos\phi \\ a\tilde{\xi}\tilde{\eta}\sin\phi \\ a\sqrt{(\tilde{\xi}^2-1)(1-\tilde{\eta}^2)} \end{pmatrix} = \begin{pmatrix} a\cosh\xi\cos\eta\cos\phi \\ a\cosh\xi\cos\eta\sin\phi \\ a\sinh\xi\sin\eta \end{pmatrix} \tag{3.22}$$

and metric scale factors

$$h_\xi = h_\eta = a\sqrt{(\sinh\xi)^2 + (\sin\eta)^2}, \qquad h_\phi = a\cosh\xi\cos\eta. \tag{3.23}$$
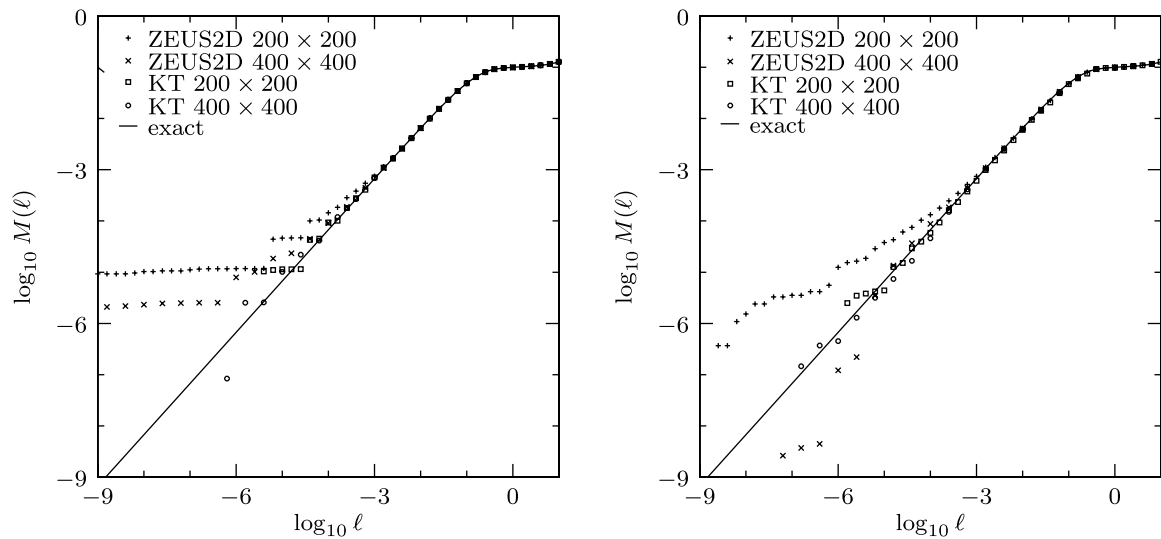
Fig. 3.13. Mass spectrum of specific angular momentum. Comparison with the ZEUS2D code at times $t = 0.4$ (left) and $t = 0.6$ (right) for different resolutions.
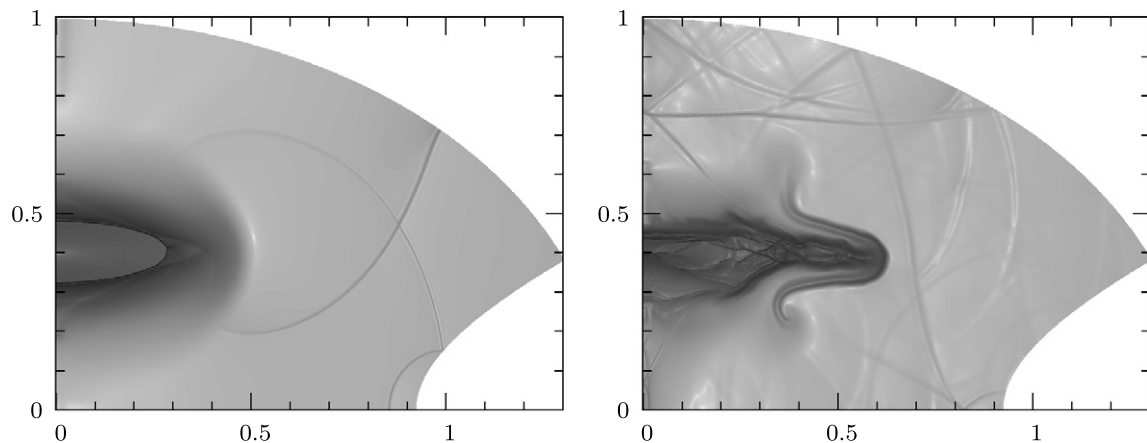

Fig. 3.14. Schlieren type images showing the absolute value of the density gradient at times $t = 0.2$ (left) and $t = 0.4$ (right). The numerical solution was computed on an oblate spheroidal mesh with a resolution of 800×800 grid cells; scales are identical to those in Fig. 3.4.

The factor a is a scaling constant which is set to unity in our calculations. If we assume symmetry with respect to the coordinate ϕ, the system of two-dimensional Euler equations is again given by (1.7) with flux vectors (3.1) and source terms (3.3). One easily proves by derivation of the scale factors that none of the commutator coefficients vanishes. Therefore all geometrical source terms have to be taken into account.

We examine the solution for the same initial condition as described in the previous chapter. The Gaussian pulse with peak density $\varrho_{max} = 10$ is located on the axis and embedded in an ambient medium with constant density $\varrho_{min} = 10^{-2}$. The whole computational domain is initialised with constant angular velocity $\Omega_0 = 10$ and constant pressure $p_0 = 1$. All boundaries are treated as reflecting walls. The only difference to the test setup on the cylindrical mesh is the shape of the computational domain with spatial extension $(\xi, \eta) \in [0, 0.88] \times [\pi/8, \pi/2]$. As for the cylindrical mesh the resolution is 800×800.

For comparison with the simulations on cylindrical grids (see Fig. 3.4) the numerical results for the density gradient are depicted in Fig. 3.14. At time $t = 0.2$ the solutions on the oblate spheroidal mesh are almost identical to those on the cylindrical mesh. There are small differences regarding the reflection of shock waves at the outer boundaries. The influence of these disturbances on the main features becomes more important at later times (see right panel). Waves reflected backwards interact with the instabilities mentioned in the previous chapter in a different way. Thus the solutions diverge more and more. This does not affect the mass spectrum in a considerable manner (see Fig 3.15). As for the cylindrical grid we observe that the spectrum is preserved very well up to $t = 0.4$. Diffusive transport at later times seems to alter the results in a similar way in either of the two curvilinear schemes.

4. Conclusions

The main advantage of central-upwind schemes is their simplicity. Apart from the propagation speeds of the non-linear waves no other information about the conservation laws under investigation is required. Therefore these schemes are applicable to a variety of physical problems. Although the solution of the Euler equations for gas dynamics is a major objective, one may also consider to solve the equations for ideal magneto-hydrodynamics or the Hamilton-Jacobi equations (see [11,33,34]). In this paper we extend this generality to non-cartesian systems, thus providing the ability to solve systems of hyperbolic conservation laws on orthogonal curvilinear grids.
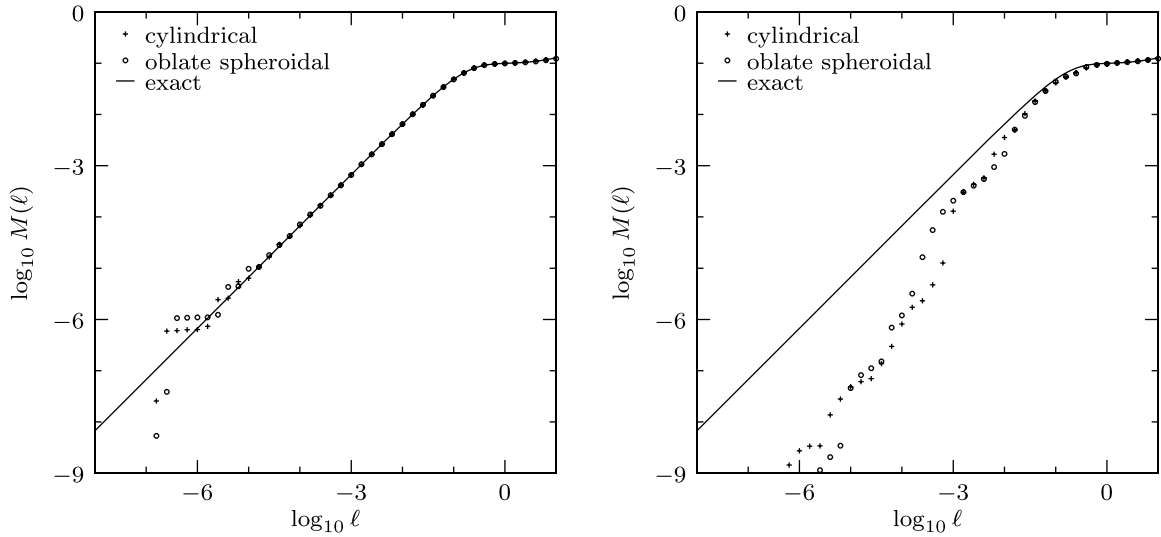
Fig. 3.15. Mass spectrum of specific angular momentum. Comparison of the results for cylindrical and oblate spheroidal grids at different times $t = 0.4$ (left) and $t = 1.0$ (right); the resolution of the simulations is 800×800.

A computer program written in `Fortran 95` has been developed in order to test the new numerical schemes [35]. So far the program is capable of solving the equations of inviscid gas dynamics in cartesian, polar, cylindrical, spherical and oblate spheroidal coordinates. In case of rotational symmetry the transport of angular momentum is included. Both quadrature rules for computation of fluxes and source terms are implemented. We performed excessive tests to verify the correctness of the numerical results. Some of them are presented in this paper. The solutions of two-dimensional Riemann problems discussed in Sections 3.1 and 3.2 are in good agreement with the cartesian results presented by other authors [1,19,20,22].

So far tests which check the detailed conservation of angular momentum are very rare in the literature. Norman et al. [23] perform a test similar to our setup, but they use a moving grid and include selfgravity in their calculations. The significance of these results is limited due to the fact that they study the mass spectrum at less than a time of circulation. Therefore we proposed a pure hydrodynamical test with angular momentum transport in Section 3.3.3. A comparison with the ZEUS-2D code [27] demonstrates that our numerical scheme leads to better results with less diffusive angular momentum transport.

Appendix A. Commutator coefficients

For orthogonal coordinate systems all off-diagonal elements in the metric tensor vanish and the infinitesimal squared distance ds^2 is written in terms of metric coefficients and infinitesimal coordinate displacements according to

$$ds^2 = g_{ij}\, dx^i\, dx^j = (h_\xi\, d\xi)^2 + (h_\eta\, d\eta)^2 + (h_\phi\, d\phi)^2. \tag{A.1}$$

Hence one might define a set of orthonormal basis vectors by

$$\widehat{e}_{\hat\xi} = \frac{1}{h_\xi} \frac{\partial}{\partial\xi}, \qquad \widehat{e}_{\hat\eta} = \frac{1}{h_\eta} \frac{\partial}{\partial\eta}, \qquad \widehat{e}_{\hat\phi} = \frac{1}{h_\phi} \frac{\partial}{\partial\phi} \tag{A.2}$$

and the corresponding set of dual 1-forms by

$$\widetilde{\omega}^{\hat\xi} = h_\xi\, d\xi, \qquad \widetilde{\omega}^{\hat\eta} = h_\eta\, d\eta, \qquad \widetilde{\omega}^{\hat\phi} = h_\phi\, d\phi. \tag{A.3}$$

Furthermore one expands all vectors, tensors and forms with respect to the new basis. Written in terms of orthonormal 1-forms the infinitesimal squared distance becomes

$$ds^2 = \left(\widetilde{\omega}^{\hat\xi}\right)^2 + \left(\widetilde{\omega}^{\hat\eta}\right)^2 + \left(\widetilde{\omega}^{\hat\phi}\right)^2 = \delta_{\hat k\hat l}\,\widetilde{\omega}^{\hat k}\widetilde{\omega}^{\hat l}, \tag{A.4}$$

i.e. the metric coefficients are independent of the coordinates. Therefore all derivatives of the metric with respect to coordinates vanish and the affine connection is determined by

$$\Gamma^{\hat k}_{\hat i\hat j} = \frac{1}{2} g^{\hat k\hat l}(c_{\hat l\hat i\hat j} + c_{\hat l\hat j\hat i} - c_{\hat i\hat j\hat l}), \tag{A.5}$$

where $g^{\hat k\hat l}$ is the inverse metric and $c_{\hat l\hat i\hat j}$ denote the commutator coefficients defined by means of the Lie-bracket

$$[\widehat{e}_{\hat i}, \widehat{e}_{\hat j}] = c^{\hat k}_{\hat i\hat j}\widehat{e}_{\hat k} = g^{\hat k\hat l} c_{\hat i\hat j\hat l}\widehat{e}_{\hat k}. \tag{A.6}$$

To obtain the commutator coefficients for the orthonormal basis mentioned above we have to apply the Lie-bracket of two basis vectors on an arbitrary function and carry out the derivatives.

$$[\widehat{e}_{\hat{\xi}}, \widehat{e}_{\hat{\eta}}] f(\xi, \eta, \phi) = \frac{1}{h_\xi} \frac{\partial}{\partial \xi} \left(\frac{1}{h_\eta} \frac{\partial}{\partial \eta} f \right) - \frac{1}{h_\eta} \frac{\partial}{\partial \eta} \left(\frac{1}{h_\xi} \frac{\partial}{\partial \xi} f \right)$$

$$= \left(-\frac{1}{h_\xi h_\eta} \frac{\partial h_\eta}{\partial \xi} \right) \frac{1}{h_\eta} \frac{\partial f}{\partial \eta} + \left(\frac{1}{h_\eta h_\xi} \frac{\partial h_\xi}{\partial \eta} \right) \frac{1}{h_\xi} \frac{\partial f}{\partial \xi}$$

$$= (c_{\hat{\xi}\hat{\eta}\hat{\eta}} \widehat{e}_{\hat{\eta}} + c_{\hat{\xi}\hat{\eta}\hat{\xi}} \widehat{e}_{\hat{\xi}}) f.$$

The non-vanishing commutator coefficients are therefore given by

$$c_{\hat{\eta}\hat{\xi}\hat{\eta}} = -c_{\hat{\xi}\hat{\eta}\hat{\eta}} = \frac{1}{h_\eta h_\xi} \frac{\partial h_\eta}{\partial \xi}, \qquad c_{\hat{\phi}\hat{\xi}\hat{\phi}} = -c_{\hat{\xi}\hat{\phi}\hat{\phi}} = \frac{1}{h_\phi h_\xi} \frac{\partial h_\phi}{\partial \xi},$$

$$c_{\hat{\xi}\hat{\eta}\hat{\xi}} = -c_{\hat{\eta}\hat{\xi}\hat{\xi}} = \frac{1}{h_\xi h_\eta} \frac{\partial h_\xi}{\partial \eta}, \qquad c_{\hat{\phi}\hat{\eta}\hat{\phi}} = -c_{\hat{\eta}\hat{\phi}\hat{\phi}} = \frac{1}{h_\phi h_\eta} \frac{\partial h_\phi}{\partial \eta},$$

$$c_{\hat{\xi}\hat{\phi}\hat{\xi}} = -c_{\hat{\phi}\hat{\xi}\hat{\xi}} = \frac{1}{h_\xi h_\phi} \frac{\partial h_\xi}{\partial \phi}, \qquad c_{\hat{\eta}\hat{\phi}\hat{\eta}} = -c_{\hat{\phi}\hat{\eta}\hat{\eta}} = \frac{1}{h_\eta h_\phi} \frac{\partial h_\eta}{\partial \phi}. \qquad (A.7)$$

References

[1] A. Kurganov, E. Tadmor, Numer. Methods Partial Differential Equations 18 (2002) 584.
[2] S.K. Godunov, Math. Sb. 47 (1959) 271.
[3] A. Kurganov, E. Tadmor, J. Comput. Phys. 160 (2000) 241.
[4] B. van Leer, J. Comput. Phys. 23 (1977) 276 (A new approach to numerical convection).
[5] A. Harten, J. Comput. Phys. 49 (1983) 357.
[6] A. Harten, P.D. Lax, B. van Leer, SIAM Rev. 25 (1983) 35.
[7] P.K. Sweby, SIAM J. Numer. Anal. 21 (1984) 995.
[8] B. van Leer, MUSCL, a new approach to numerical gas dynamics, in: Computing in Plasma Physics and Astrophysics, Max-Planck-Gesellschaft, Max-Planck-Institut für Plasmaphysik, Garching, Germany, 1976, p. E1.
[9] R. Mönchmeyer, E. Müller, Astron. Astrophys. 217 (1989) 351.
[10] E.A. Lufkin, J.F. Hawley, Astrophys. J. Suppl. 88 (1993) 569.
[11] A. Kurganov, S. Noelle, G. Petrova, SIAM J. Sci. Comput. 23 (2001) 707.
[12] C. Hirsch, Fundamentals of Numerical Discretization, Numerical Computation of Internal and External Flows, vol. 1, John Wiley & Sons, Chichester, UK, 1988.
[13] A. Kurganov, C.T. Lin, Commun. Comput. Phys. 2 (2007) 141.
[14] J.M. Greenberg, A.Y. Leroux, SIAM J. Numer. Anal. 33 (1996) 1.
[15] R.J. LeVeque, J. Comput. Phys. 146 (1998) 346.
[16] C.W. Shu, SIAM J. Sci. Stat. Comput. 9 (1988) 1073.
[17] C.W. Shu, S. Osher, J. Comput. Phys. 77 (1988) 439.
[18] B. van Leer, J. Comput. Phys. 32 (1979) 101 (A second-order sequel to Godunov's method).
[19] C.W. Schulz-Rinne, J.P. Collins, H.M. Glaz, SIAM J. Sci. Comput. 14 (1993) 1394.
[20] P.D. Lax, X.-D. Liu, SIAM J. Sci. Comput. 19 (1998) 319.
[21] R. Courant, K. Friedrichs, H. Lewy, IBM J. Res. Dev. 11 (1967) 215 (Engl. translation of [36]).
[22] J.O. Langseth, R.J. LeVeque, J. Comput. Phys. 165 (2000) 126.
[23] L.M. Norman, J.R. Wilson, R.T. Barton, Astrophys. J. 239 (1980) 968.
[24] I.M. Gel'fand, G.E. Shilov, Properties and Operations, Generalized Functions, vol. 1, Academic Press, New York, 1964.
[25] J.W.S. Lord Rayleigh, Investigation of the character of the equilibrium of an incompressible heavy fluid of variable density, Proc. Lond. Math. Soc. 14 (1882) 170–177.
[26] G.I.S. Taylor, Proc. R. Soc. Lond. A 201 (1950) 192.
[27] J.M. Stone, M.L. Norman, ZEUS-2D V2.0.3, 1995; http://lca.ucsd.edu/portal/codes/zeus2d.
[28] J.M. Stone, M.L. Norman, Astrophys. J. Suppl. 80 (1992) 753.
[29] M.L. Norman, K.-H.A. Winkler, 2-D Eulerian hydrodynamics with fluid interfaces, self-gravity and rotation, in: Astrophysical Radiation Hydrodynamics, D. Reidel, 1986, pp. 187–221.
[30] J. von Neumann, R.D. Richtmyer, J. Appl. Phys. 21 (1950) 232.
[31] W.M. Tscharnuter, K.-H.A. Winkler, Comput. Phys. Comm. 18 (1979) 171.
[32] M. Abramowitz, I.A. Stegun, Handbook of Mathematical Functions with Formulas, Graphs, and Mathematical Tables, Applied Mathematics Series, vol. 55, National Bureau of Standards, US Gov. Print. Office, Washington, DC, 1964.
[33] J. Balbás, E. Tadmor, C.-C. Wu, J. Comput. Phys. 201 (2004) 261.
[34] J. Balbás, E. Tadmor, SIAM J. Sci. Comput. 28 (2006) 533.
[35] T.F. Illenseer, Fosite software, 2007; http://fosite.sourceforge.net.
[36] R. Courant, K. Friedrichs, H. Lewy, Math. Ann. 100 (1928) 32.